

PENETRATION RESISTANCE OF 4340 STEEL/POLYUREA LAMINATE

by

Vishnu Vardhan Kumar Pajjuri

A thesis submitted to the faculty of
The University of North Carolina at Charlotte
in partial fulfillment of the requirements
for the degree of Master of Science in
Mechanical Engineering

Charlotte

2017

Approved by:

Dr. Alireza Tabarraei

Dr. Ronald E. Smelser

Dr. Tony L. Schmitz

ABSTRACT

VISHNU VARDHAN KUMAR PAJJURI. Penetration resistance of 4340 steel/polyurea laminate. (Under the direction of DR. ALIREZA TABARRAEI)

Enhancement of the penetration resistance of materials used in the defense industry is of great interest since such improvements can save human life and can reduce the loss of resources caused by high velocity projectiles penetrating through the walls of important weaponry such as tanks, choppers and armored personnel carriers. Recent experimental studies have shown that polymer coatings can improve the ballistic limit of steel plates. Experimental study of the ballistic properties are expensive but a computational model can make this study more affordable. For accurate modeling of ballistic impact problems, our finite model considers the impact of large deformations, high strain rates and steep hikes in temperatures on the properties of the system.

In this thesis we use finite element analysis to study the ballistic properties of steel-polyurea laminate. The FEM simulations are conducted in Abaqus and includes a projectile impacting a target. We use 4340 steel plate with and without polyurea coating as the target. The material behavior of 4340 steel target plate is captured by Mie-Grüneisen and Johnson-Cook models and Mooney-Rivlin model is used to model the behavior of polyurea and adhesive. The projectile is assumed to be rigid. Various scenarios involving different types of projectiles and different positions of the polyurea are studied.

After careful examination of the results, it is concluded that failure occurs in two different modes (petalling and shearing). The failure mode depends on impact velocities. It is also observed that polyurea coating improves the penetration resistance and the energy absorption rate of 4340 steel plate. Finally it is noted that the shape of the projectile has its impact on the material failure and the effect of polyurea.

ACKNOWLEDGEMENTS

I would like to thank my advisor Dr. Alireza Tabarraei, for his guidance and motivation, without which this thesis would not have been possible. His teachings have always been useful and have given encouragement.

It would be my duty to extend my gratitude to the committee members Dr. Ronald E. Smelser and Dr. Tony L. Schmitz for taking their time to be on my committee and assess my work.

I am thankful to my friends in my lab, in UNCC and elsewhere for their support throughout this journey.

DEDICATION

I dedicate this work to my parents, Mr and Mrs. Venkateshwarlu and Chandrakala and my sister, Lakshmi Durga who offer their unconditional love and support and have always been there for me while I chase my dream.

TABLE OF CONTENTS

LIST OF FIGURES	ix
LIST OF TABLES	xiv
LIST OF ABBREVIATIONS	1
CHAPTER 1: Introduction	1
CHAPTER 2: Projectiles And Scenarios	6
CHAPTER 3: Theory	12
3.1. Mie-Grüneisen equation of state model	12
3.2. Isotropic elastic model	14
3.3. Johnson-Cook plasticity model	14
3.4. Johnson-Cook damage model	15
3.5. Mooney-Rivlin model	16
3.6. Simple damage model	17
3.7. Conservation of Energy	18
CHAPTER 4: MODELLING IN ABAQUS	19
4.1. Property module	19
4.1.1. Material properties of 4340 steel	19
4.1.2. Material properties of polyurea	20
4.1.3. Adhesive	21
4.1.4. Projectiles	21
4.2. Mesh module	22
4.2.1. Seeding	22

4.2.2.	Meshing techniques	22
4.2.3.	Element type	24
4.2.4.	Aspect ratio	26
4.3.	Assembly module	27
4.4.	Interaction module	27
4.5.	Step module	28
4.5.1.	Solver	29
4.6.	Boundary conditions & Predefined fields	30
4.7.	Output request	30
4.8.	Python Scripting in Abaqus	30
CHAPTER 5: Comparison and results		32
5.1.	Comparison	32
5.2.	Results	34
5.3.	Pointed nose projectile	35
5.3.1.	Pointed nose projectile on blank 4340 steel plate	35
5.3.2.	Comparing the residual velocities and energy absorption of blank plate, polyurea backed, polyurea sandwiched and polyurea front plates impacted by pointed nose projectile	38
5.3.3.	Best energy absorption for pointed nose projectile	39
5.4.	Jacket nose projectile	42
5.4.1.	Jacket nose projectile on blank 4340 steel plate	42
5.4.2.	Comparing the residual velocities and energy absorption of blank plate, polyurea backed, polyurea sandwiched and polyurea front plates with jacket nose projectile	44

5.4.3.	Best energy absorption for jacket nose projectile	45
5.5.	Round nose projectile	47
5.5.1.	Round nose projectile on blank 4340 steel plate	47
5.5.2.	Comparing the residual velocities and energy absorption of blank plate, polyurea backed, polyurea sandwiched and polyurea front plates with round nose projectile	49
5.5.3.	Best energy absorption for round nose projectile	51
5.6.	Flat nose projectile	53
5.6.1.	Flat nose projectile on blank 4340 steel plate	53
5.6.2.	Comparing the residual velocities and energy absorption of blank plate, polyurea backed, polyurea sandwiched and polyurea front plates with flat nose projectile	55
5.6.3.	Best energy absorption for flat nose projectile	56
5.7.	Angle of impact	58
5.8.	Sensitivity analysis	60
CHAPTER 6: Summary and Conclusion		62
REFERENCES		64

LIST OF FIGURES

FIGURE 1.1: Polyurea formation	1
FIGURE 1.2: True stress-strain curve of polyurea [1]	2
FIGURE 1.3: True stress-strain curve of 4340 steel [2]	3
FIGURE 2.1: Different orientations of the steel and polyurea composite with respect to bullet impact direction. (a) represents a blank plate, (b) represents polyurea coated on the backside of the plate, (c) represents polyurea sandwiched between the steel plates, (d) represents polyurea coated on the front side of the plate.	6
FIGURE 2.2: Different projectiles used in this study	7
FIGURE 2.3: Different scenarios considered in this study for targets impacted by pointed nose projectile. (a) pointed nose onto blank plate, (b) pointed nose onto polyurea backed plate, (c) pointed nose onto polyurea sandwiched plate, (d) pointed nose onto polyurea front plate.	8
FIGURE 2.4: Different scenarios considered in this study for targets impacted by jacket nose projectile. (a) jacket nose onto blank plate, (b) jacket nose onto polyurea backed plate, (c) jacket nose onto polyurea sandwiched plate, (d) jacket nose onto polyurea front plate.	9
FIGURE 2.5: Different scenarios considered in this study for targets impacted by round nose projectile. (a) round nose onto blank plate, (b) round nose onto polyurea backed plate, (c) round nose onto polyurea sandwiched plate, (d) round nose onto polyurea front plate.	9
FIGURE 2.6: Different scenarios considered in this study for targets impacted by flat nose projectile. (a) flat nose onto blank plate, (b) flat nose onto polyurea backed plate, (c) flat nose onto polyurea sandwiched plate, (d) flat nose onto polyurea front plate.	10
FIGURE 2.7: Scenario of normal impact and inclined impact by pointed nose projectile on to blank plate. (a) normal impact onto blank plate, (b) inclined impact onto blank plate.	10
FIGURE 2.8: a) composite, b) steel plate, c) adhesive, d) polyurea	11
FIGURE 4.1: Swept meshing on a round nose bullet	23

FIGURE 4.2: Bottom-up meshing of the polyurea (top left), the adhesive (top right) and the 4340 steel plate (bottom).	24
FIGURE 4.3: Shape change of a material block under a bending moment in the ideal situation [3]	25
FIGURE 4.4: Shape change of the fully integrated first order element under a bending moment which shows shearlocking [3]	25
FIGURE 4.5: Shape change of the reduced integrated first order element under a bending moment which shows hourglassing [3]	26
FIGURE 4.6: Master surface penetration into the slave surface in a pure master-slave contact [4]	28
FIGURE 5.1: A comparison of the petalling behavior of the blank plate impacted by the pointed nose projectile at low velocities [1]	32
FIGURE 5.2: A comparison of the shearing behavior of the blank steel plate impacted by the pointed nose projectile at high velocities [1]	33
FIGURE 5.3: A comparison of the behavior of the polyurea coated to the front side of the steel plate impacted by the flat nose projectile at a high velocity, (left) experimental [5], [6] and (right) numerical	34
FIGURE 5.4: Petalling of blank 4340 plate impacted by a pointed nose projectile at a velocity of 335 m/s. Fringe plot is equivalent plastic strain, PEEQ.	35
FIGURE 5.5: Shear plugging of blank 4340 plate impacted by a pointed nose projectile at a velocity of 430 m/s. Fringe plot is equivalent plastic strain, PEEQ.	36
FIGURE 5.6: Residual velocities of pointed nose projectile after impacting blank 4340 steel plate.	37
FIGURE 5.7: Energy absorption of the blank 4340 steel plate impacted by pointed nose projectile.	38
FIGURE 5.8: Residual velocities of pointed nose projectile impacting blank plate, polyurea backed, polyurea sandwiched and polyurea front plates.	39

FIGURE 5.9: Energy absorption of blank plate, polyurea backed, polyurea sandwiched and polyurea front plates impacted by pointed nose projectile.	40
FIGURE 5.10: Residual velocities of pointed nose projectile impacting blank plate and polyurea backed steel plate.	40
FIGURE 5.11: Energy absorption of blank plate and polyurea backed steel plate impacted by pointed nose projectile.	41
FIGURE 5.12: Damage progression for polyurea backed 4340 steel plate impacted by pointed nose projectile at a velocity of 360 m/s. Fringe plot is von Mises stress.	41
FIGURE 5.13: Residual velocities of jacket nose projectile after impacting blank 4340 steel plate	42
FIGURE 5.14: Energy absorption of blank 4340 steel plate after impacted by jacket nose projectile.	43
FIGURE 5.15: Shear plugging of blank 4340 plate impacted by a jacket nose projectile at a velocity of 410 m/s. Fringe plot is equivalent plastic strain, PEEQ.	43
FIGURE 5.16: Residual velocities of jacket nose projectile impacting blank plate, polyurea backed, polyurea sandwiched and polyurea front plates.	44
FIGURE 5.17: Energy absorption of blank plate, polyurea backed, polyurea sandwiched and polyurea front plates impacted by jacket nose projectile	45
FIGURE 5.18: Residual velocities of jacket nose projectile impacting blank plate and polyurea backed steel plate.	46
FIGURE 5.19: Energy absorption of blank plate and polyurea backed steel plate impacted by jacket nose projectile.	46
FIGURE 5.20: Damage progression for polyurea backed 4340 steel plate impacted by jacket nose projectile at a velocity of 360 m/s. Fringe plot is von Mises stress.	47
FIGURE 5.21: Residual velocities of round nose projectile after impacting blank 4340 steel plate	48

FIGURE 5.22: Energy absorption of blank 4340 steel plate impacted by round nose projectile.	48
FIGURE 5.23: Shear plugging of blank 4340 plate impacted by round nose projectile at a velocity of 360 m/s. Fringe plot is equivalent plastic strain, PEEQ.	49
FIGURE 5.24: Residual velocities of round nose projectile impacting blank plate, polyurea backed, polyurea sandwiched and polyurea front plates.	50
FIGURE 5.25: Energy absorption of blank plate, polyurea backed, polyurea sandwiched and polyurea front plates impacted by round nose projectile	50
FIGURE 5.26: Residual velocities of round nose projectile impacting blank plate and polyurea backed steel plate.	51
FIGURE 5.27: Energy absorption of blank plate and polyurea backed steel plate impacted by round nose projectile	52
FIGURE 5.28: Damage progression for polyurea backed 4340 steel plate impacted by round nose projectile at a velocity of 360 m/s. Fringe plot is von Mises stress.	52
FIGURE 5.29: Residual velocities of flat nose projectile after impacting blank 4340 steel plate.	53
FIGURE 5.30: Energy absorption of blank 4340 steel plate impacted by flat nose projectile.	54
FIGURE 5.31: Shear plugging of blank 4340 plate impacted by flat nose projectile at a velocity of 360 m/s. Fringe plot is equivalent plastic strain, PEEQ.	54
FIGURE 5.32: Residual velocities of flat nose projectile impacting blank plate, polyurea backed, polyurea sandwiched and polyurea front plates.	55
FIGURE 5.33: Energy absorption of blank plate, polyurea backed, polyurea sandwiched and polyurea front plates impacted by flat nose projectile	56

FIGURE 5.34: Residual velocities of flat nose projectile impacting blank plate and polyurea backed steel plate.	57
FIGURE 5.35: Energy absorption of blank plate and polyurea backed steel plate impacted by flat nose projectile	57
FIGURE 5.36: Damage progression for polyurea backed 4340 steel plate impacted by flat nose projectile at a velocity of 390 m/s.	58
FIGURE 5.37: Residual velocities of the normal impact and inclined impacts of a pointed nose projectile on a blank steel plate	59
FIGURE 5.38: Energy absorption of the normal impact and inclined impacts of a blank steel plate impacted by pointed nose projectile.	59
FIGURE 5.39: Section view of the damage progression of inclined pointed nose projectile impacting a blank 4340 steel plate at 360 m/s. Fringe plot is equivalent plastic strain, PEEQ	60
FIGURE 5.40: Change in strain to fracture with errors in the parameters	60
FIGURE 5.41: Change in the ballistic limits of the blank 4340 steel plate impacted by pointed nose projectile as a function of percentage error of the parameters.	61

LIST OF TABLES

TABLE 1.1: Chemical composition of 4340 steel [7]	4
TABLE 4.1: Material parameters of 4340 steel for the Mie-Grüneisen EOS model [8]	20
TABLE 4.2: Material parameters of 4340 steel for the Johnson-Cook plasticity model [2]	20
TABLE 4.3: Material parameters of 4340 steel for the Johnson-Cook dynamic failure model [9]	20
TABLE 4.4: Material parameters of polyurea for Mooney-Rivlin hyperelastic model [1]	21
TABLE 4.5: Material parameters of polyurea for damage model [1]	21

CHAPTER 1: Introduction

Improving the penetration resistance of materials such as 4340 steel is of high importance to defense and aeronautics. Such materials are used in combat equipment like tanks, choppers and containers subjected to hostile environments. To improve its penetration resistance, it is fundamental to understand the behavior of such materials under impact and ballistic loading conditions which involve high strain rates, high temperatures and large deformations.

Many techniques have been proposed for the enhancement of the strength of 4340 steel and application of polymer coatings is one of the most promising technique. In this study, the effect of polyurea coating on the improvement of the penetration resistance and energy absorption of 4340 steel is studied. Polyurea is an elastomeric polymer which has gained a lot of attention because of its high fracture strain which allows it to deform more while absorbing and dissipating the energy and has low density which makes its weight less and insignificant when added onto the components. These polymer coatings are used for a wide range of applications on both civil and military structures to reduce failure and fragmentation of the structures.

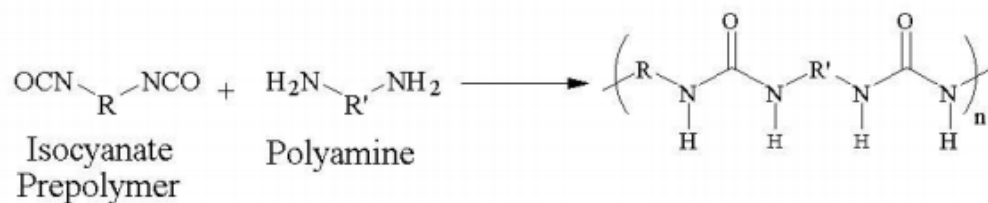


Figure 1.1: Polyurea formation

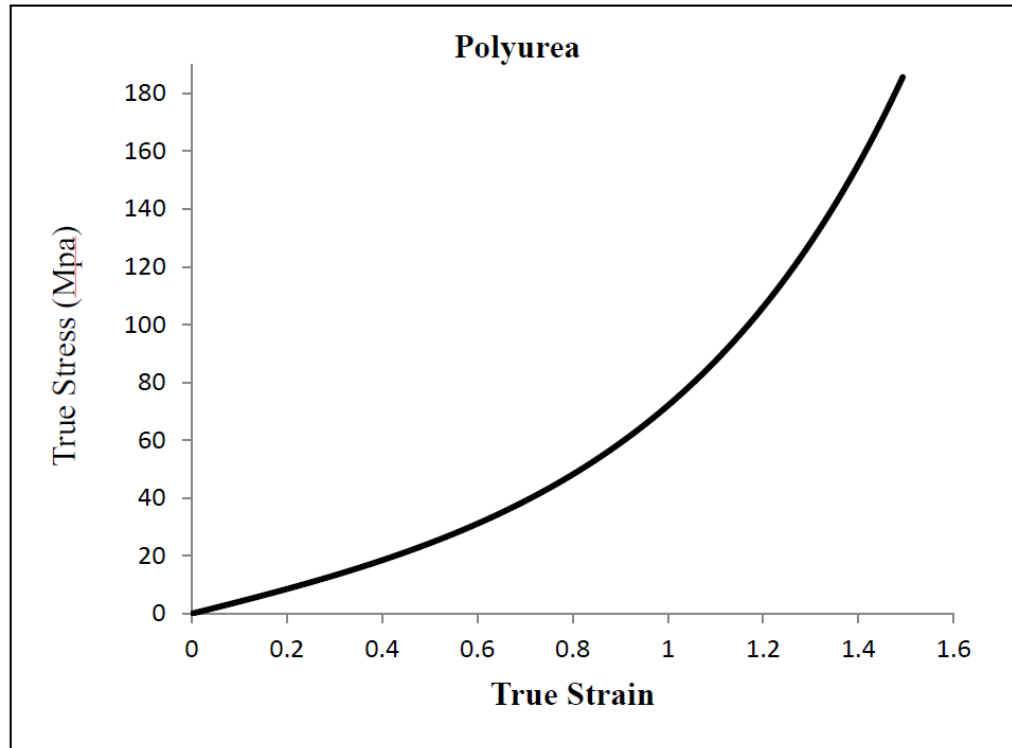


Figure 1.2: True stress-strain curve of polyurea [1]

Many experimental studies have been conducted on the response of blank steel plates and steel-polyurea laminated composites subjected to dynamic conditions [10]. The thermo-viscoplastic behavior of various structural steels at wide range of strain rates and temperatures has been carried out and different constitutive models are compared in [11]. The effect of the shape of the projectiles on the behavior of thin steel plates is carried out by Arias et al [12]. A computational assessment of ballistic impact of steel/polyurea laminate composite plate with coating on the back side of the plate was carried out in [13]. The behavior of polyurea when subjected to high loading rates and their transition from rubbery state to glass state is studied by Grujicic et al [14].

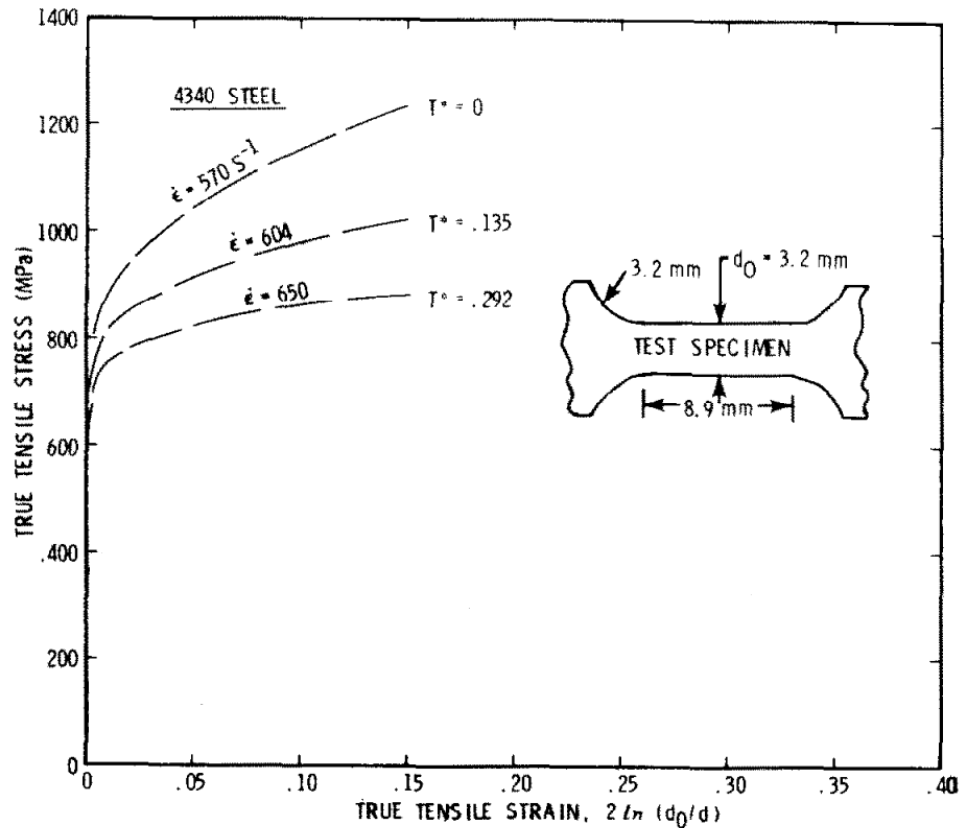


Figure 1.3: True stress-strain curve of 4340 steel [2]

The polyurea's ability to increase the penetration resistance and to reduce the fragmentation of the underlying structure is discussed by Xue et al [1]. In their computational study Xue et al showed that the penetration resistance of a steel plate increases by 42% when it is coated with polyurea on its backside. The fragmentation of steel plates is also greatly reduced upon the addition of the polyurea. Polyurea can also be used to damp the pressure waves generated from blast loading and increase their energy absorption of the structures. Like most metals, the material properties of steel change under high strain rate and temperature. Nasser and Guo [15] studied the behavior of steel at a range of temperatures from 77K to 8000K and strain rates in the range of 0.01/s to 8000/s and showed that steel displays high ductility and fracture strength at high strain rates and low temperatures.

Table 1.1: Chemical composition of 4340 steel [7]

Fe	Ni	Cr	Mn	C	Mo	Si	S	P
95-96	1.65-2.00	0.7-0.9	0.6-0.8	0.37-0.43	0.2-0.3	0.15-0.3	0.04	0.035

The energy absorption benefit of polyurea is not restricted to metals/polyurea coating alone. Ceramics, concrete and other structural materials can be coated with polyurea to increase their penetration resistance from the projectiles. Yadav et al [16] showed that polyurea plays a major role in mitigating the crack propagation and fragmentation of the ceramic structures.

Understanding the mechanism of ballistic impact which involves high strain rates, high temperatures and pressure waves through experimental studies is not only very challenging but very expensive. On the other hand, Computational model can capture such dynamic behaviors at a much shorter time span. The research conducted on the penetration resistance of 4340 steel-polyurea laminate is limited and no computational studies is found to study the effects of the shape of projectile on the optimal position of polyurea coating on the steel plate.

In this thesis, the effect of polyurea coating on the penetration resistance of the steel impacted by different shaped projectiles is studied. The Mie-Grüneisen equation of state model is used to capture the effects of stress wave propagation in steel. Johnson-Cook plasticity model is used to calculate the flow stress needed to capture the plastic deformations. Johnson-Cook dynamic failure model is used to capture the failure of steel. The hyperelastic behavior of polyurea and adhesives is modeled using the Mooney-Rivlin constitutive model.

Chapter 2 shows different scenarios used in this study. Chapter 3 discusses the constitutive models used to model the behavior of different materials used in the study. Chapter 4 contains the description and the process of modeling in Abaqus. The behavior of the materials from the finite element model is compared with exper-

iments in chapter 5 and the simulation results are presented in chapter 5.2. Finally a summary and conclusion of this study are given in chapter 6.

CHAPTER 2: Projectiles And Scenarios

In thesis, we first study the impact of projectile on blank 4340 steel plate and then a plate coated with polyurea on its back, polyurea sandwiched between plates and polyurea coating in front of plate to know the effect of the position of polyurea coating on the penetration resistance. Different targets used in this study are shown in figure 2.1.

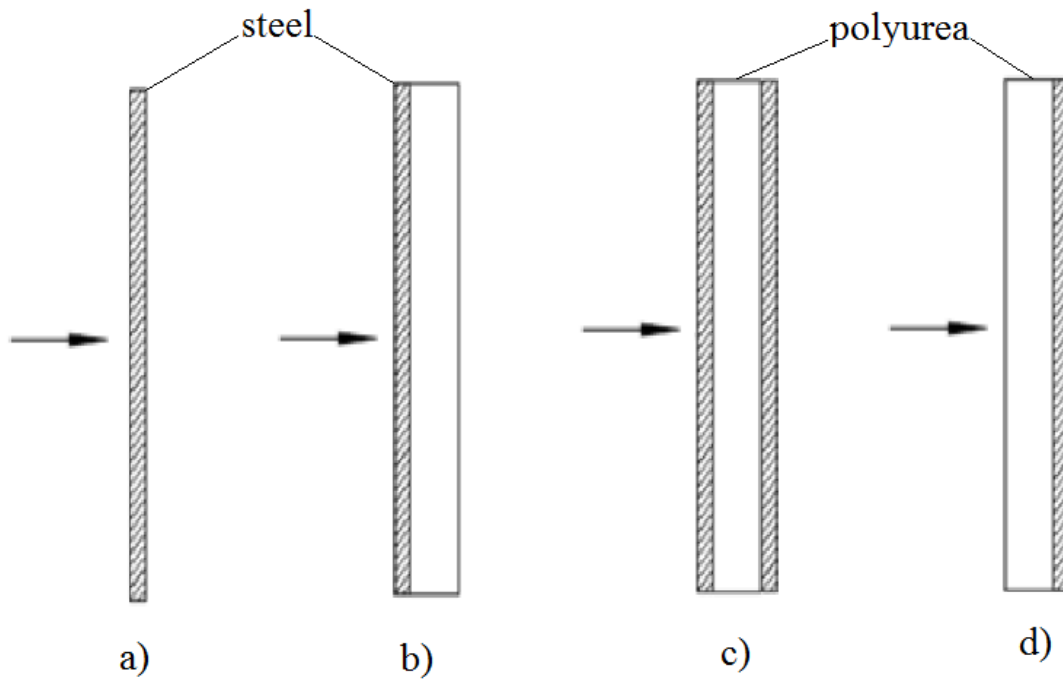
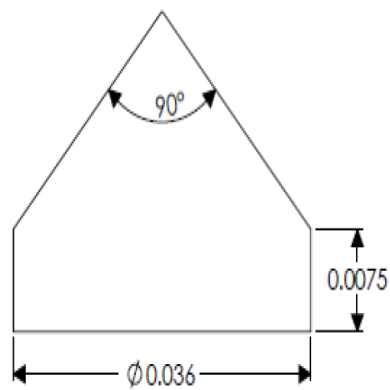
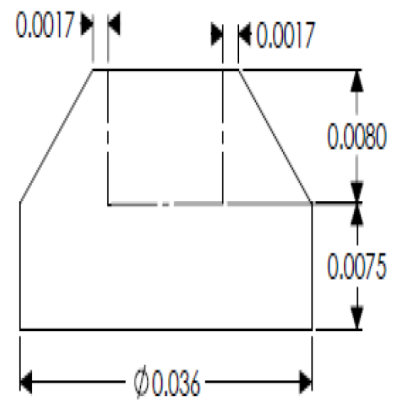


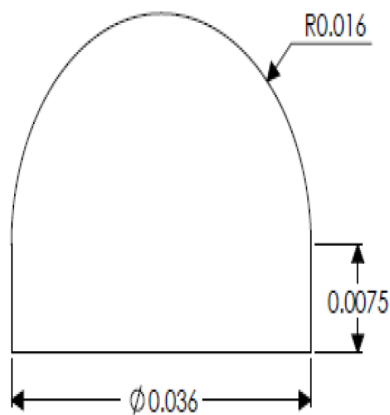
Figure 2.1: Different orientations of the steel and polyurea composite with respect to bullet impact direction. (a) represents a blank plate, (b) represents polyurea coated on the backside of the plate, (c) represents polyurea sandwiched between the steel plates, (d) represents polyurea coated on the front side of the plate.



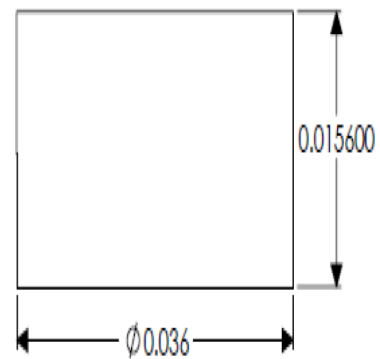
(a) Pointed nose projectile



(b) Jacket nose projectile



(c) Round nose projectile



(d) Flat nose projectile

Figure 2.2: Different projectiles used in this study

The effect of projectile shape on the ballistic properties of steel/polyurea composite is studied by considering projectiles of different shapes. Figure 2.2 shows all types of projectiles used in this study along with their dimensions. All the projectiles have a mass of 0.145 Kg and a diameter of 0.036 m. The steel plate has a diameter 0.01523 m and thickness 0.0047625 m while the thickness of polyurea is 0.01176 m and the

thickness of the adhesive attaching polyurea to plate is 0.0005 m.

Figure 2.3 shows a pointed nose projectile impacting a blank plate, a polyurea backed plate, a polyurea sandwiched plate and a polyurea front plate.

Figure 2.4 shows the second scenario where a jacket nose projectile impacts a blank steel plate, a polyurea backed plate, a polyurea sandwiched plate and a polyurea front plate.

Figure 2.5 shows the third scenario where a round nose projectile goes on to impact a blank steel plate, a polyurea backed plate, a polyurea sandwiched plate and a polyurea front plate.

Figure 2.6 shows the fourth scenario where a flat nose projectile impacts a blank steel plate, a polyurea backed plate, a polyurea sandwiched plate and a polyurea front plate.

The impact of the penetration angle on the ballistic properties are studied by modeling a pointed nose projectile impacting with an inclination of 30° to the plate. This is shown in figure 2.7

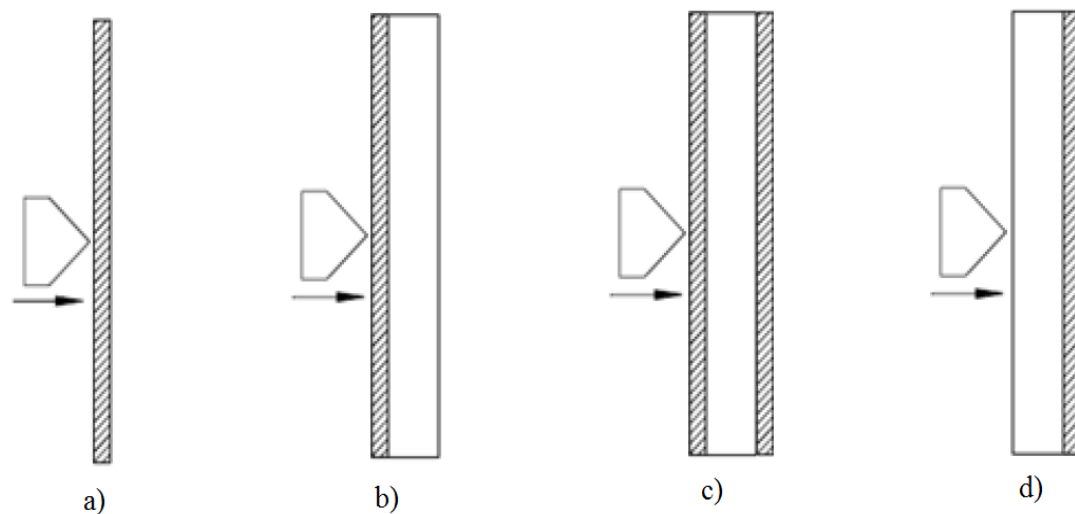


Figure 2.3: Different scenarios considered in this study for targets impacted by pointed nose projectile. (a) pointed nose onto blank plate, (b) pointed nose onto polyurea backed plate, (c) pointed nose onto polyurea sandwiched plate, (d) pointed nose onto polyurea front plate.

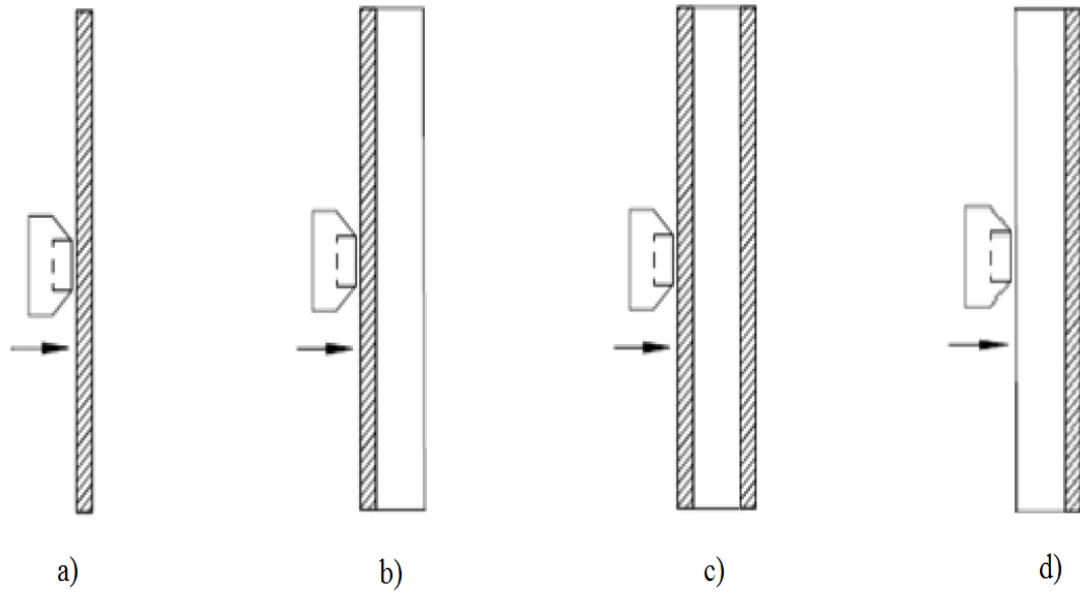


Figure 2.4: Different scenarios considered in this study for targets impacted by jacket nose projectile. (a) jacket nose onto blank plate, (b) jacket nose onto polyurea backed plate, (c) jacket nose onto polyurea sandwiched plate, (d) jacket nose onto polyurea front plate.

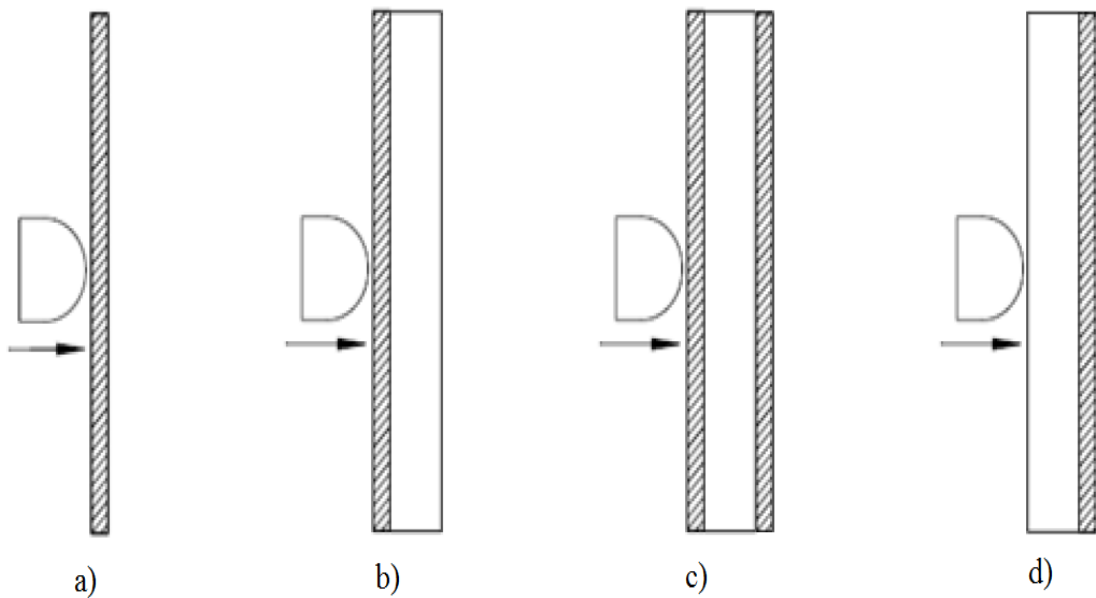


Figure 2.5: Different scenarios considered in this study for targets impacted by round nose projectile. (a) round nose onto blank plate, (b) round nose onto polyurea backed plate, (c) round nose onto polyurea sandwiched plate, (d) round nose onto polyurea front plate.

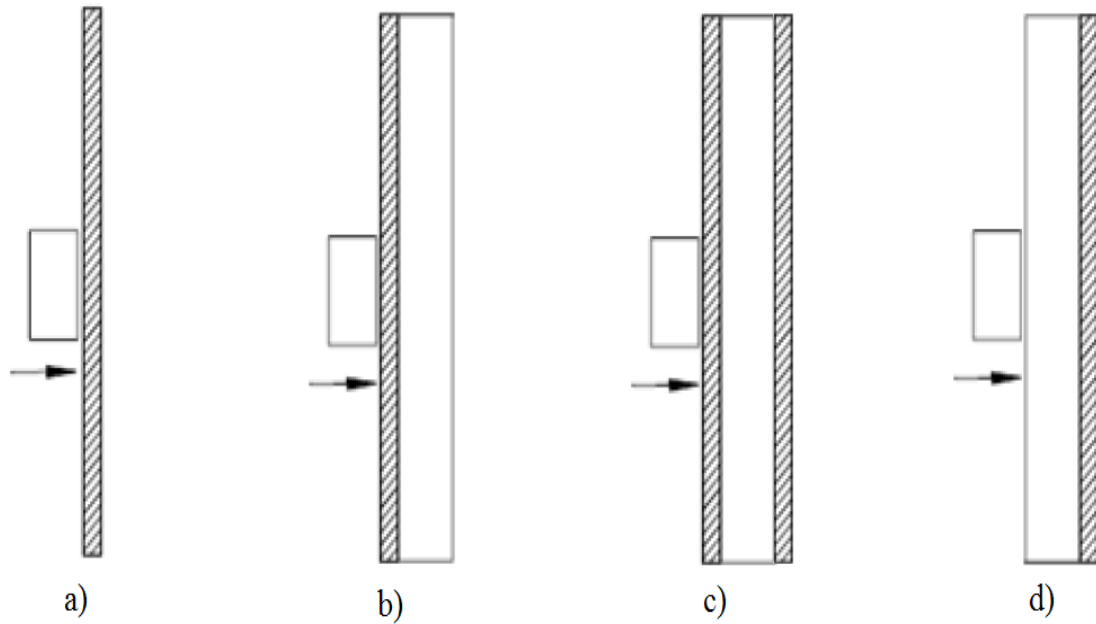


Figure 2.6: Different scenarios considered in this study for targets impacted by flat nose projectile. (a) flat nose onto blank plate, (b) flat nose onto polyurea backed plate, (c) flat nose onto polyurea sandwiched plate, (d) flat nose onto polyurea front plate.

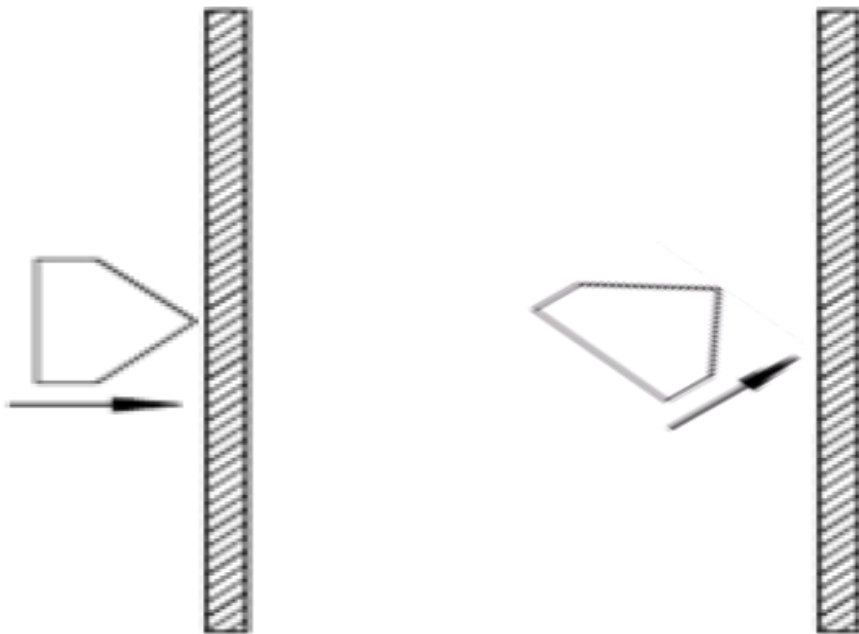


Figure 2.7: Scenario of normal impact and inclined impact by pointed nose projectile on to blank plate. (a) normal impact onto blank plate, (b) inclined impact onto blank plate.

Figure 2.8 shows the composite target in this study and the separation of the composite into layers.

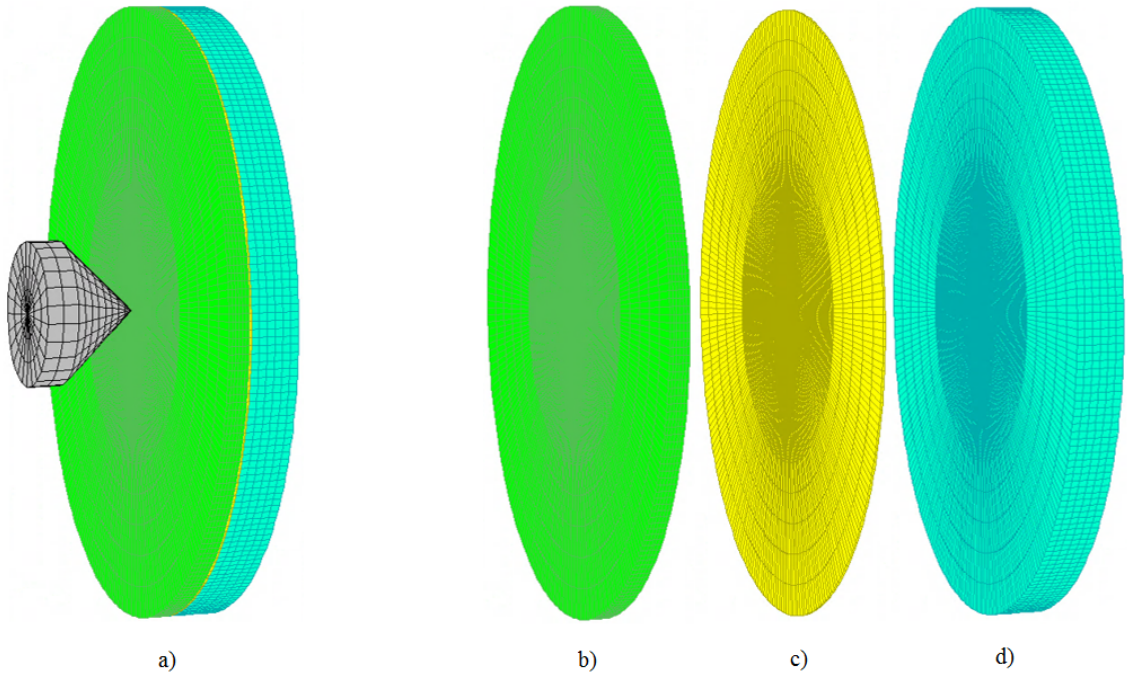


Figure 2.8: a) composite, b) steel plate, c) adhesive, d) polyurea

CHAPTER 3: Theory

Numerical simulation of a complex problem such as a high velocity projectile impacting a target which involves large deformations, strain rates and high temperatures must employ equation of states and constitutive models that has the capability of correctly capturing the material responses. Abaqus/Explicit has a variety of tools and constitutive models to model these type of simulations.

3.1 Mie-Grüneisen equation of state model

When a pressure generated by shock wave propagation exceeds the material strength by several orders of magnitude, the early stages of material response can be regarded as hydrodynamic, strength effects appear in the late stages of the event [18]. The Mie-Grüneisen equation of state model captures the volumetric behavior of the material response under impact loading. Generally, an equation of state (EOS) describes the pressure in a material as a function of both density and temperature. But in case of high impact problems, the thermodynamic state is so rapid that there is no time for the heat to be transferred, in such adiabatic conditions, the Mie-Grüneisen EOS [19] is used to predict pressure in solid.

Mie-Grüneisen equation of state assumes that pressure is a function of the current density, ρ , and the internal energy per unit mass, E_m .

$$p = f(\rho, E_m) \tag{3.1}$$

where p is the pressure stress, ρ is the current density and E_m is the internal energy per unit mass. Mie-Grüneisen equation of state is linear in energy and the equation

3.1 becomes:

$$p - p_H = \Gamma \rho (E_m - E_H) \quad (3.2)$$

where p_H is Hugoniot pressure which is a function of density and is obtained by fitting experimental data. Γ is the Grüneisen ratio defined as

$$\Gamma = \Gamma_0 \frac{\rho_0}{\rho} \quad (3.3)$$

where Γ_0 is Grüneisen material constant and ρ_0 is the reference density. The Hugoniot energy, E_H from equation 3.2 can be calculated from the Hugoniot pressure as

$$E_H = \frac{p_H \eta}{2\rho_0} \quad (3.4)$$

where $\eta = 1 - \frac{\rho_0}{\rho}$ is the nominal volumetric compressive strain. A common fit to the Hugoniot data is given by

$$p_H = \frac{\rho_0 c_0^2 \eta}{(1 - s\eta)^2} \quad (3.5)$$

where c_0 and s define the relation between the shock velocity, U_s , and the particle velocity, U_p , as follows:

$$U_s = c_0 + sU_p \quad (3.6)$$

Substituting all the above equations in equation 3.2, we end up on the $U_s - U_p$ Mie-Grüneisen equation which is used in Abaqus and the Mie-Grüneisen material parameters for 4340 steel is given in table 4.1.

$$p = \frac{\rho_0 c_0^2 \eta}{(1 - s\eta)^2} \left(1 - \frac{\Gamma_0 \eta}{2}\right) + \Gamma_0 \rho_0 E_m \quad (3.7)$$

3.2 Isotropic elastic model

The above mentioned Mie-Grüneisen equation of state captures only the volumetric behavior of the material and needs a constitutive model that captures its deviatoric behavior in the elastic phase. This is where the elastic shear model comes into play. In this model, the elastic shear behavior is defined by relating the deviatoric stress to the deviatoric strain as

$$S = 2\mu e^{el} \quad (3.8)$$

where S is the deviatoric stress, e^{el} is the deviatoric strain and μ is the elastic shear modulus.

3.3 Johnson-Cook plasticity model

Johnson-Cook plasticity model is used to capture the plastic phase of the 4340 steel plate. It perfectly captures the effects of high strain rates and high temperatures and expresses the flow stress required to plastically deform the plate as a function of plastic strain, strain rate and temperature [2]. The Johnson-Cook relationship is expressed as:

$$\bar{\sigma} = [A + B(\bar{\epsilon}^{pl})^n] \left[1 + C \ln \left(\frac{\dot{\bar{\epsilon}}^{pl}}{\dot{\epsilon}_0} \right) \right] [1 - (T^*)^m] \quad (3.9)$$

where A , B , n , C and m are the material constants, $\bar{\sigma}$ is the von Mises flow stress, $\bar{\epsilon}^{pl}$ is the equivalent plastic strain, $\dot{\bar{\epsilon}}^{pl}$ is the equivalent plastic strain rate, $\dot{\epsilon}_0 = 1.0s^{-1}$ is the reference strain rate and T^* is the homologous temperature defined as

$$T^* = \begin{cases} 0 & \text{for } T < T_{transition} \\ \frac{(T - T_{transition})}{(T_{melt} - T_{transition})} & \text{for } T_{transition} \leq T \leq T_{melt} \\ 1 & \text{for } T > T_{melt} \end{cases}$$

where T is the current temperature, $T_{transition}$ is the transition temperature or the reference temperature at which the material parameters are to be measured, T_{melt} is

the melting temperature of the material beyond which the material melts and becomes a fluid.

In the Johnson-Cook model the effects of strain, strain rate and temperature are present in three different brackets but their product effectively captures the flow stress. The expression in the first set of brackets represent the stress as function of strain where A is the yield stress and B and n are the strain hardening factors. The second bracket represents the strain rate effects where C is the strain rate parameter and the last bracket captures the temperature effects where m is the thermal parameter. All the parameters are calibrated by manipulating the curves obtained from tension, torsion and compression tests at the required strain rates and temperatures.

3.4 Johnson-Cook damage model

Johnson-Cook damage model is a dynamic damage model, which means an element fails instantaneously without any stiffness left in it. This is in contrast with the progressive models which allow smooth degradation of material stiffness. This model is chosen only when dealing with very high strain rates and temperatures. The damage of an element is determined by a material damage parameter, ω and is defined as [4]

$$\omega = \frac{\bar{\varepsilon}_0^{pl} + \sum \Delta \bar{\varepsilon}^{pl}}{\bar{\varepsilon}_f^{pl}} \quad (3.10)$$

where $\bar{\varepsilon}_0^{pl}$ is the initial equivalent plastic strain if any, $\Delta \bar{\varepsilon}^{pl}$ is the increment equivalent plastic strain at the end of every increment and $\bar{\varepsilon}_f^{pl}$ is the equivalent strain at fracture. The element is allowed to fail if its ω reaches or exceeds 1.

The strain at fracture, $\bar{\varepsilon}_f^{pl}$ is proposed to be a function of the triaxial stress state, the plastic strain rate and the homologous temperature [9] and is given by

$$\bar{\varepsilon}_f^{pl} = [d_1 + d_2 \exp(d_3 \sigma^*)] \left[1 + d_4 \ln \left(\frac{\dot{\bar{\varepsilon}}^{pl}}{\dot{\varepsilon}_0} \right) \right] [1 + d_5 T^*] \quad (3.11)$$

where d_1, d_2, d_3, d_4 and d_5 are the material constants that are to be calculated at the transition temperature, $T_{transition}$ and the reference strain rate, $\dot{\epsilon}_0$. The dimensionless pressure-stress ratio, σ^* is defined as

$$\sigma^* = \frac{\sigma_m}{\sigma_{eq}} \quad (3.12)$$

where σ_m is the mean stress or pressure stress and is the average of the three principal stresses, whereas σ_{eq} is the von Mises equivalent stress.

The equation mentioned above for the strain at fracture differs from the original [9] only in the sign of d_3 as it is observed that the strain at fracture increases with increase in pressure-stress ratio, so d_3 is assigned positive sign and is very important to be rectified as wrong sign may yield unwanted results. When the failure criteria is met, that is when the damage parameter, ω cumulates and adds upto 1, then the load carrying capacity of the element is assumed to be zero for the rest of the analysis.

3.5 Mooney-Rivlin model

The polyurea and adhesive are highly incompressible material and are treated as rubber-like materials and modeled using hyperelastic models. These hyperelastic materials are described using strain energy potential, $U(\epsilon)$ which is the strain energy per unit volume stored in the material and is function of strain at that point. The form of Mooney-Rivlin is defined as

$$U = C_{10}(\bar{I}_1 - 3) + C_{01}(\bar{I}_2 - 3) + \frac{1}{D_1}(J^{el} - 1)^2 \quad (3.13)$$

where U is the strain energy per unit reference volume, C_{10}, C_{01} and D_1 are the material parameters, J^{el} is the elastic volume ratio. \bar{I}_1 and \bar{I}_2 are the first invariant and second invariant of the deviatoric strain and is defined as

$$\bar{I}_1 = \bar{\lambda}_1^2 + \bar{\lambda}_2^2 + \bar{\lambda}_3^2 \quad (3.14)$$

and

$$\bar{I}_2 = \bar{\lambda}_1^{(-2)} + \bar{\lambda}_2^{(-2)} + \bar{\lambda}_3^{(-2)} \quad (3.15)$$

where the deviatoric stretches, $\bar{\lambda}_i$ is given by

$$\bar{\lambda}_i = J^{-\frac{1}{3}} \lambda_i \quad (3.16)$$

In the above equations J is the total volume ratio and λ_i are the principal stretches. The initial shear modulus, μ_0 and bulk modulus, K_0 are given by

$$\mu_0 = 2(C_{10} + C_{01}) \quad (3.17)$$

and

$$K_0 = \frac{2}{D_1} \quad (3.18)$$

3.6 Simple damage model

For both polyurea and adhesive the damage portion of the behavior is modeled using the simple damage model. This damage model is phenomenological which means the values are observed from the experiments and given as an input, in our case the fracture strain, $\bar{\varepsilon}_f^{pl}$ is inputted into the model and when the equivalent plastic strain, $\bar{\varepsilon}^{pl}$ adds up to the specified value, the element is considered to fail. In this thesis, the temperature effects on the polyurea are not considered. As in section 3.4, the material reaches damage initiation when the following condition is satisfied.

$$\omega_D = \int \frac{d\bar{\varepsilon}^{pl}}{\bar{\varepsilon}_f^{pl}(\eta, \dot{\varepsilon}^{pl})} = 1 \quad (3.19)$$

3.7 Conservation of Energy

Law of conservation of energy states that *energy can neither be created nor be destroyed, rather is converted from one form to another*. In continuum mechanics terms when only mechanical energy is considered, this law of conservation of energy can be derived as [20]

$$P = \dot{K} + \dot{U} \quad (3.20)$$

where P is the external work done by the surface and body forces, \dot{K} is the change in the kinetic energy of the system and \dot{U} is the change in the internal energy.

In this study, the external work done by the bullet is equal to the change in its kinetic energy. The energy is transferred to the plate by changing the kinetic energy of the plate and the internal strain energy of the plate. The change in the internal energy can be attributed to the deformations or the failure of the material. The change in kinetic energy of the plate is small and is not considered in this study. Therefore equation 3.20 as follows

$$P = \dot{U} \quad (3.21)$$

where P is the change in the kinetic energy of the bullet and is given by

$$P = \frac{1}{2}mv_i^2 - \frac{1}{2}mv_r^2 \quad (3.22)$$

where m is the mass of the bullet, v_i is the initial velocity of the bullet and v_r is the residual velocity of the bullet.

CHAPTER 4: MODELLING IN ABAQUS

Modelling in Abaqus starts with sketching the parts in the part module which is followed by property module where the material models are created which are assigned to sections. These sections are then assigned to the parts generated in the part module before seeding and meshing. The parts are assembled in the assembly module and interactions between the parts are created. Constraints, loads and boundary conditions are given to the assembly and the required output is requested. Finally the type of analysis is selected and a job is created and submitted for analysis.

4.1 Property module

The property module is used to define the behavior of materials used in the model. The accuracy of the results obtained from the simulations depends on the accuracy of equation of material inputs given to the models.

4.1.1 Material properties of 4340 steel

The behavior of 4340 steel is modeled using Mie-Grüneisen equation of state model which captures its early volumetric behavior. The parameters for this model are calibrated by Steinberg, D.J [8] and are summarized in the table 4.1. Since the problem deals with high strain rates and temperatures, the plasticity portion is modeled using Johnson-Cook plasticity model. The Johnson-Cook parameters for the 4340 steel are carefully calibrated by Johnson, G.R and Cook, W.H [2] and are given in table 4.2. The damage and failure behavior of the 4340 steel is modeled using Johnson-Cook Damage model with its parameters calibrated by Johnson, G.R. and Cook, W.H [9] and are provided in the table 4.3

Table 4.1: Material parameters of 4340 steel for the Mie-Grüneisen EOS model [8]

Density, ρ [kg/m^3]	Grüneisen coefficient, Γ_0	Parameter, c_0 [m/s]	Parameter, s	Reference temperature, [K]	Specific heat, c [$J/(kg\ K)$]
7830	1.67	4578	1.33	293	477

Table 4.2: Material parameters of 4340 steel for the Johnson-Cook plasticity model [2]

A [MPa]	B [MPa]	n	θ_{melt} [K]	$\theta_{transition}$ [K]	m	C	$\dot{\epsilon}_0$ [$1/s$]
792	510	0.26	1793	293	1.03	0.014	1

Table 4.3: Material parameters of 4340 steel for the Johnson-Cook dynamic failure model [9]

d_1	d_2	d_3	d_4	d_5	θ_{melt} [K]	$\theta_{transition}$ [K]	$\dot{\epsilon}_0$ [$1/s$]
0.05	3.44	2.12	0.002	0.61	1793	293	1

4.1.2 Material properties of polyurea

Polyurea is an elastomer and is being modeled as a hyper-elastic material using the Mooney-Rivlin model whose parameters are given in table 4.4. C.M. Roland et al. [17] found out that polyurea exhibits strain rate hardening effect from simple tension tests at high strain rates. The peak strain rate at the centre of the plate is found to be $10,000\ s^{-1}$. The fracture strain of 1.5 at higher strain rates is calibrated by extrapolating the curves [1] obtained by C.M. Roland et al. The effects of change in strain rate and change in temperature are not considered in this study. The

damage behavior of the polyurea is modeled using a simple damage model and all the concerned material parameters are summarized in the table

Table 4.4: Material parameters of polyurea for Mooney-Rivlin hyper-elastic model [1]

C_{10} [MPa]	C_{01} [MPa]	K [GPa]	ν	Density, ρ [kg/m ³]
4.5	0.7	2.57	0.486	1250

Table 4.5: Material parameters of polyurea for damage model [1]

ε_f	$\frac{\cdot pl}{\varepsilon}$
1.5	10,000

4.1.3 Adhesive

An extra bonding mechanism between Polyurea and 4340 steel plate is necessary to keep them together at such high strain rates. Therefore a strong adhesive material is used to bond these two surfaces. This adhesive material is considered to have the same hyper-elastic behavior as the polyurea but slightly different failure parameters. The fracture strain of the adhesive is calibrated to be 1.3, slightly less than the polyurea to match the results from the simulations with the experimental results.

4.1.4 Projectiles

All the projectiles are considered as rigid bodies and therefore do not need any materials to be assigned to them. We ignore the negligible deformations of the projectiles in this study. Also modeling the projectiles which are not the focus of this study as rigid bodies reduces the computational cost as rigid bodies have no more than 6 degrees of freedom unlike other elements which have more degrees of freedom.

4.2 Mesh module

After the parts are sketched and the material properties assigned, now its time to mesh the parts of the model. The mesh module has all the tools required to mesh different parts of the assembly. The process of meshing involves seeding, selecting the right mesh techniques and element types.

4.2.1 Seeding

Seeds are the divisions made along the edges of the part to specify the mesh density of the part. Selecting the edges and specifying the number of seeds, uniformly divides the edge in equal parts. If different mesh densities are needed on the same edge then the edge should be partitioned and then seeded.

4.2.2 Meshing techniques

Abaqus provides a variety of meshing techniques to mesh models of different topologies. In this thesis, swept meshing technique and bottom-up meshing technique are used. These meshing techniques can be selected while assigning the mesh controls to the parts.

4.2.2.1 Swept meshing

Swept meshing for a solid element works by replicating a source side along an edge to the target side. In this work, the swept mesh is used to mesh the projectiles and also the source side of the bottom-up mesh. To mesh the projectiles, a revolved swept mesh is used where the source side is revolved a full 360° and uses the quad-dominated element shape option as shown in figure 4.1.

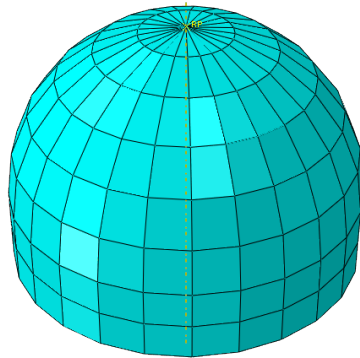


Figure 4.1: Swept meshing on a round nose bullet

4.2.2.2 Bottom-up meshing

Bottom-up meshing is a manual, incremental meshing process that allows to build a hexahedral mesh in any solid region. While all top-down meshing techniques are tied directly to the geometry, bottom-up mesh relaxes this constraint allowing the mesh to ignore some geometric features. The steel plate, polyurea and adhesive are meshed using this technique. First a source side of two dimensional mesh is generated using the swept meshing as mentioned in section 4.2.2.1, then using sweep option the connecting sides along which the mesh is swept from the source side to the target side.

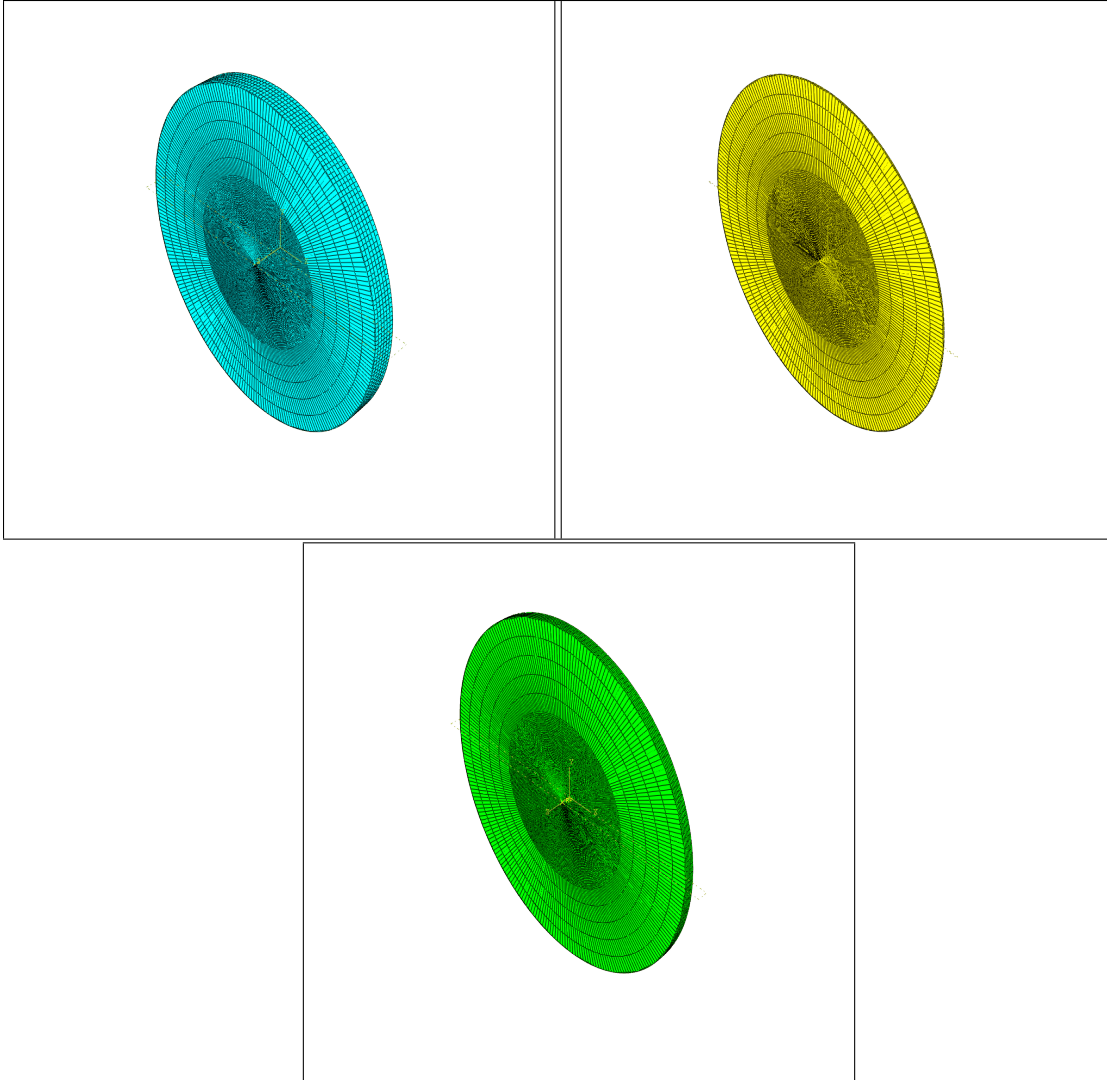


Figure 4.2: Bottom-up meshing of the polyurea (top left), the adhesive (top right) and the 4340 steel plate (bottom).

4.2.3 Element type

Abaqus offers a wide variety of element types in its extensive element library for solving a wide range of problems. Selecting the proper element for the analysis is important. In this thesis, 4340 steel plate, adhesive and polyurea are meshed using linear hexahedral and wedge elements. C3D8R which is a continuum three dimensional 8-node reduced integration hexahedral elements and C3D6 which is a continuum three dimensional 6 node wedge elements are used. A linear element

is chosen over second-order elements as the former gives satisfactory results in the Abaqus/Explicit.

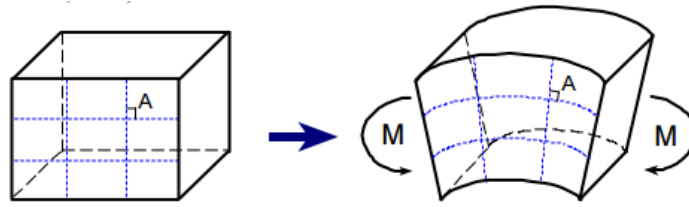


Figure 4.3: Shape change of a material block under a bending moment in the ideal situation [3]

Reduced integration elements counter the effects of shear locking which are evident in the fully integrated elements [3] as shown in fig 4.4. But on the other hand, reduced integration elements has its own difficulties in the form of hourglassing which makes the elements too flexible. Fig 4.5 shows the effect of hourglassing, but this is partly controlled in Abaqus by providing hourglass control mechanisms and its effects can be almost nullified by using a reasonably fine mesh. Reduced integration elements uses a lower order integration to form stiffness matrices than the full integration elements. Hence using reduced integration elements reduces the computational time. For example, in this study a C3D8R element with a single integration point scheme is used instead of the C3D8 element with 8 integration points, thereby reducing the computational time of the former to less than 30% of the later, thus drastically reducing the computational cost.

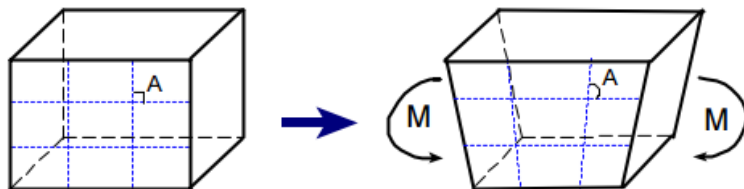


Figure 4.4: Shape change of the fully integrated first order element under a bending moment which shows shearlocking [3]

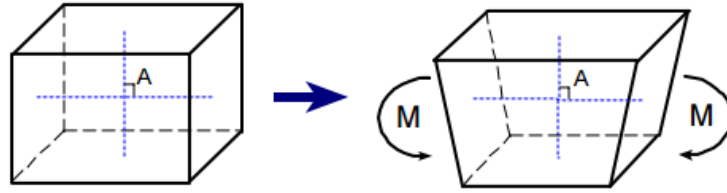


Figure 4.5: Shape change of the reduced integrated first order element under a bending moment which shows hourglassing [3]

C3D6 wedge elements are used to mesh the regions which cannot be meshed by tetrahedral elements, in this case, the center of the plate, adhesive and polyurea. The accuracy of wedge elements is not as high as the tetrahedral elements and should be used with a very fine mesh to get good results. R3D4 rigid quadrilateral elements are used to mesh all the projectiles since the deformation of projectile is not the area of interest.

4.2.4 Aspect ratio

Aspect ratio is the ratio between the longest side of the element to its shortest side. For a higher accuracy, it is recommended that the aspect ratio of all the elements in the model be kept close to unity. But in this case, since the plate is circular, achieving an aspect ratio close to one is not possible. But efforts have been made to keep the aspect ratio of the elements of interest to be less than 10 which is reasonable. In the course of this study, it was observed that aspect ratio does indeed play an important role in yielding good results.

Having a reasonably fine mesh is very important for having good results. A coarse mesh may produce excessive distortion in an element and may distort the results. The 4340 steel plate and the polyurea are meshed fine with 6 elements each through their thickness and the adhesive is meshed with 1 element. The total number of elements for the combined model of 4340 steel/adhesive/polyurea is 178,750.

4.3 Assembly module

In the next step all the part instances are assembled together using position constraints to align the edges, faces or vertices by translation or rotation. In this case, as the entire deformable body consisting of the 4340 steel plate, the adhesive and the polyurea is modeled as a single part, there are only two part instances that needed to be assembled and this is accomplished by using co-axial and face to face position constraints. After assembly, node sets and surface sets of the model are created. These sets are used later to assign the interactions and predefined fields to the model.

4.4 Interaction module

In the interaction module, the interaction between parts when they come in contact with each other is defined. In this thesis, the general contact algorithm provided in the Abaqus/Explicit is used to model the interactions between the 4340 steel plate, the adhesive, the polyurea and the projectiles. Using a proper contact formulation is very critical in this project since the predicted energy absorption significantly depends on it. The general contact algorithm is chosen over the contact pair algorithm since it is a very simple, powerful and has very few restriction on the types of surfaces that can be involved. The general contact algorithm uses finite sliding formulation which allows any arbitrary motion of the surfaces in contact. Contact properties can be assigned to govern the behavior of the surfaces when they come into contact, by default the general contact algorithm assumes hard contact in normal direction with no friction. In this study, the steel plate is given an interaction properties in both normal and tangential direction with a coefficient of friction of 0.55 and the same with polyurea with a coefficient of friction of 0.25.

The general contact formulation uses a constraint enforcement method called penalty method and has both balanced master-slave contact and pure master-slave contact methods. In this study, the pure master-slave enforcement is used which means

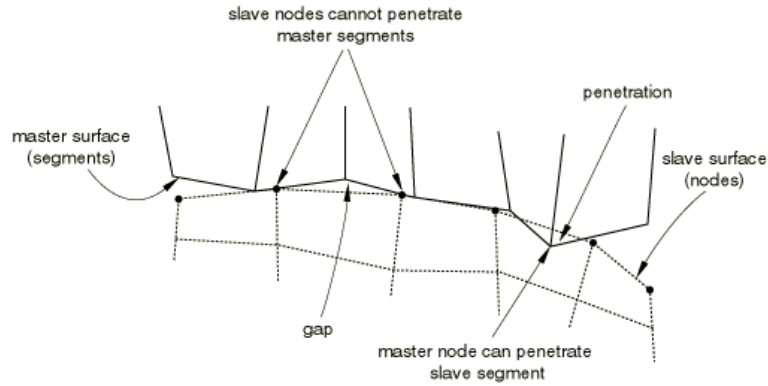


Figure 4.6: Master surface penetration into the slave surface in a pure master-slave contact [4]

the surface assigned as the master surface can penetrate through the slave surface unhindered but the slave surface cannot penetrate the master as shown in the figure 4.6. This pure master-slave method is used to define the rigid projectiles as a master and the deformable 4340 steel/adhesive/polyurea model as the slave.

4.5 Step module

The step module provides a convenient way of defining any number of analysis steps in which different loads, boundary conditions, interactions etc., can be applied to the model. In this study, explicit dynamic analysis procedure is used in conjunction with the adiabatic analysis to carry out the highly non-linear penetration problem. The high strain rates, the temperature effects and the non-linear behavior of the materials - 4340 steel, polyurea and adhesive make this study a highly nonlinear problem. The explicit dynamic analysis is chosen because it is computationally efficient for the analysis of complex models with short dynamic response times and is compatible with the general contact conditions. The adiabatic process is chosen to calculate the heat generated by the plastic work and the resulting rise in temperature and thereby to see how the temperature rise affects the temperature dependent material properties.

4.5.1 Solver

For explicit dynamic analysis, Abaqus/Explicit uses an explicit integration rule together with the use of the lumped element matrices to solve the equations of motions. In an implicit dynamic analysis, the implicit operator matrix must be inverted and a set of nonlinear equilibrium equations are to be solved at each time increment whereas in an explicit dynamic analysis like this case, the values of acceleration, velocity and displacement are calculated in terms of quantities known at the beginning of the time increment, which reduces the whole burden of inverting mass and stiffness matrices at each time increment. The following equations of motions are integrated using the central difference integration:

$$\ddot{u}_{(i)}^N = (M^{NJ})^{-1}(P_{(i)}^J - I_{(i)}^J) \quad (4.1)$$

$$\dot{u}_{(i+\frac{1}{2})}^N = \dot{u}_{(i-\frac{1}{2})}^N + \frac{\Delta t_{(i+1)} + \Delta t_{(i)}}{2} \ddot{u}_{(i)}^N \quad (4.2)$$

$$u_{(i+1)}^N = u_{(i)}^N + \Delta t_{(i+1)} \dot{u}_{(i+\frac{1}{2})}^N \quad (4.3)$$

where M^{NJ} is the mass matrix, P^J is the applied load vector, I^J is the internal force vector, u^N is a degree of freedom (displacement in this case) and i is the increment in the step.

At the beginning of the increment, the accelerations are calculated from equation 4.1 and from there the central difference integration is used to obtain velocities and displacements. The explicit dynamic analysis is vulnerable to the size of time increment since the central difference operator is conditionally stable. For stability, the stable time increment is set as the time required for a stress wave to travel across the smallest element in the model and is given by:

$$\Delta t \approx \frac{L_{min}}{c_d} \quad (4.4)$$

where L_{min} is the size of the smallest element in the model and c_d is the speed of the stress wave.

4.6 Boundary conditions & Predefined fields

Specifying appropriate boundary conditions to the model makes the model more realistic and computationally efficient. In this case, all the translational and rotational degrees of freedom of the projectiles are constrained except for one direction in which the projectiles impact the plate. This drastically reduces the number of degrees of freedom that are free and at which the computations are to be made. For the 4340 steel/adhesive/polyurea model no degree of freedom is constrained and are free to move in any and all directions.

An initial velocity is given to the projectile through the predefined fields and an initial temperature is given to the entire model including projectiles since an adiabatic analysis is being carried out.

4.7 Output request

For each analysis an appropriate field output should be requested, since the results obtained from the .odb file or the .dat file depend on the variables requested in the field output or the history output. For instance, STATUS is an important parameter that determines if an element has reached its failure point and whether it needs to be removed/eroded from the analysis. Such variables play an important role in observing the penetration process. Care has to be taken to request only the required output variables as the size of the output file and the time in writing it increases with increase in the number of variables.

4.8 Python Scripting in Abaqus

Abaqus GUI internally runs on python which is a object oriented programming language. Submitting a python script to the Abaqus/CAE kernel would generate a model in the GUI. As mentioned in section 4.2, the 4340 steel/adhesive/polyurea

model was generated as a single part and then divided into parts to assign the materials. To mesh these parts with a bottom up meshing, the graphic user interface (GUI) of the Abaqus is not well equipped. The bottom up meshing has to be done through scripting in python since a source mesh could not be created for the parts in the middle using the GUI. In this thesis a python script has been generated and is run to obtain the required model. The values of required output parameters, in this case the velocity of the projectiles at various time intervals, can also be requested to be written to a text file through a python script. This reduces the effort of post processing. Also automating the creation of multiple models through python scripting can drastically reduce the time and effort.

CHAPTER 5: Comparison and results

In this chapter, the behavior of the material from the simulations are compared to the material behaviors observed in experiments to draw similarities between them. Also the results from the simulations of all scenarios are presented.

5.1 Comparison

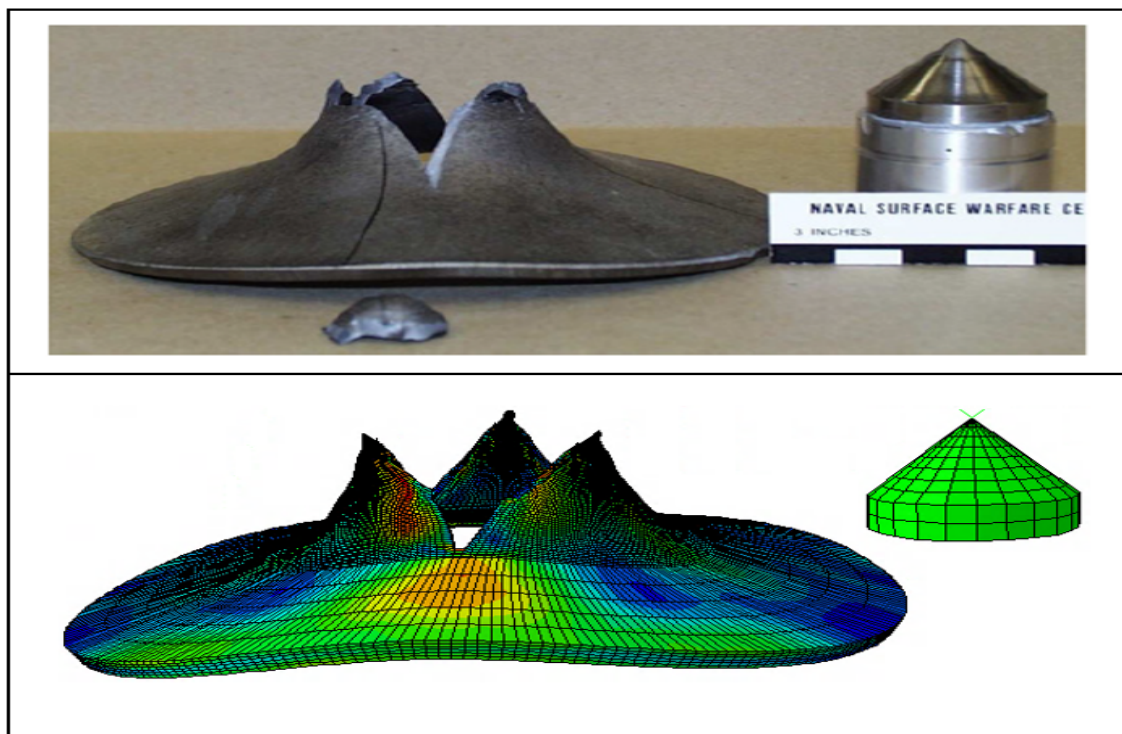


Figure 5.1: A comparison of the petalling behavior of the blank plate impacted by the pointed nose projectile at low velocities [1]

The finite element results are compared with the experimental results for a blank plate subjected to a pointed nose projectile at an impact velocity of 335 m/s. Figure 5.1 shows that the finite element model is capable of capturing the petalling mechanism observed during experiments.

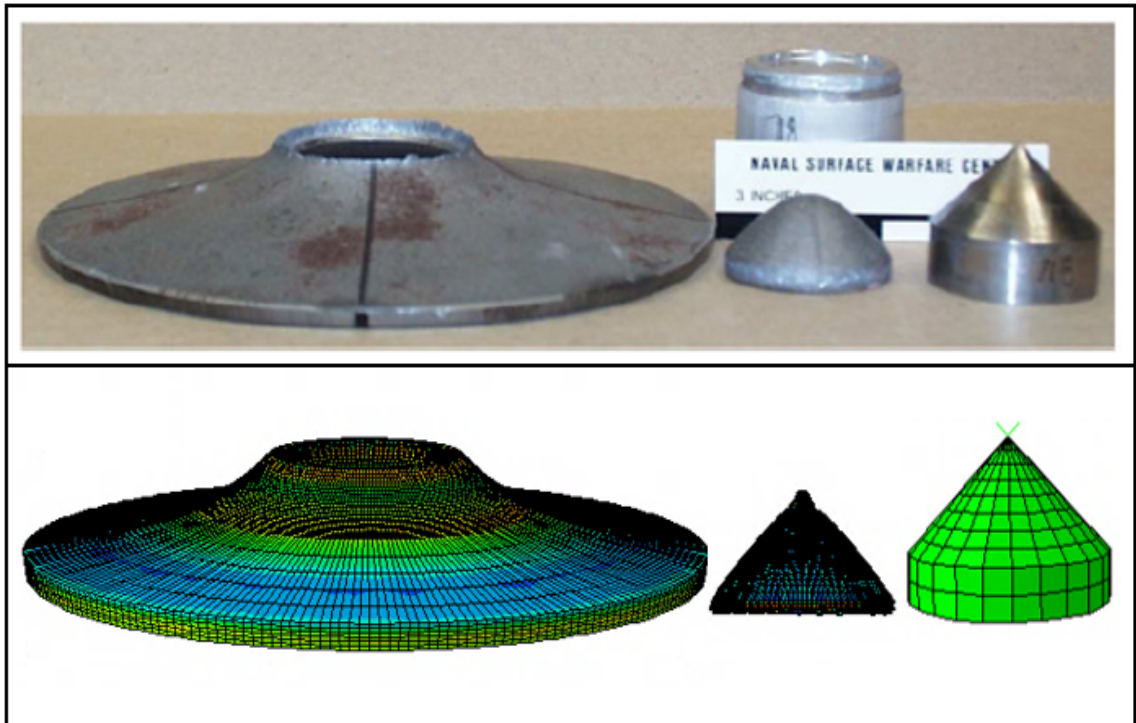


Figure 5.2: A comparison of the shearing behavior of the blank steel plate impacted by the pointed nose projectile at high velocities [1]

The finite element results are compared with the experimental results for a blank plate subjected to a pointed nose projectile at an impact velocity of 430 m/s. Figure 5.2 shows that the finite element model is capable of capturing the shear plugging mechanism observed during experiments.

Examination of the scenario of a steel plate coated with polyurea in the front impacted by flat nose projectile at high velocities in Figure 5.3 show that the behavior of the polyurea between experiments [5] and numerical simulations from the FE model is comparable and this shows that the current FE model is in good agreement with the experimental observations.

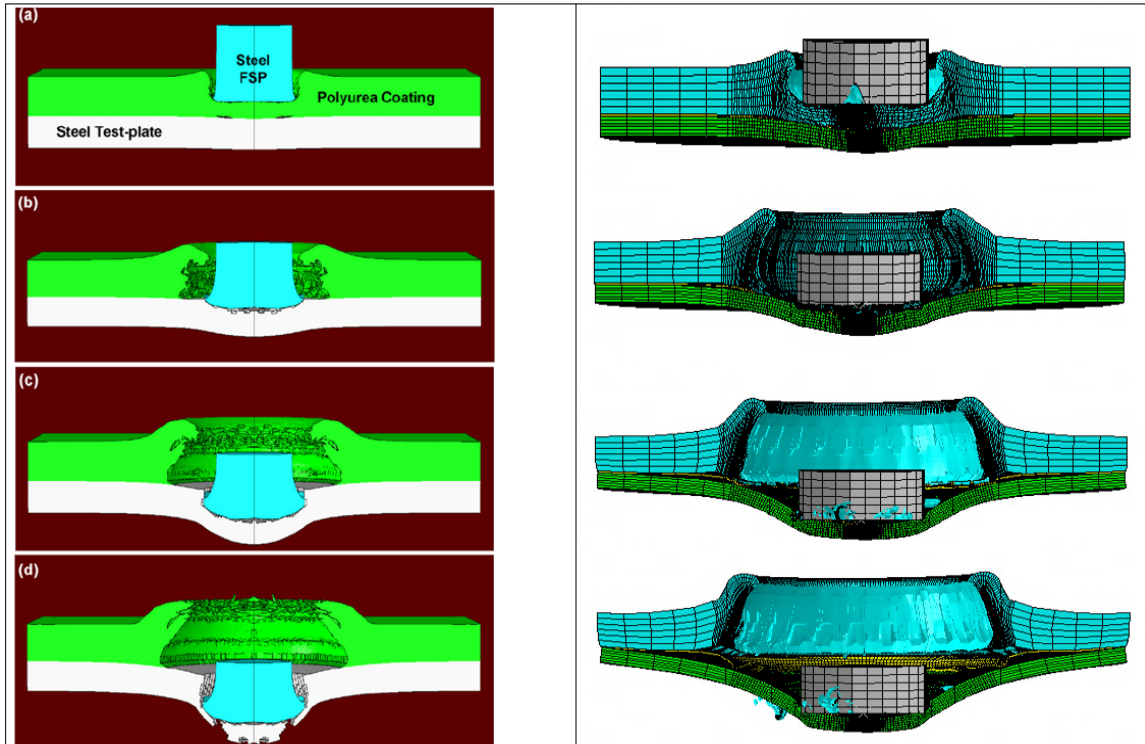


Figure 5.3: A comparison of the behavior of the polyurea coated to the front side of the steel plate impacted by the flat nose projectile at a high velocity, (left) experimental [5], [6] and (right) numerical

5.2 Results

Through out this study, the failure behavior of 4340 steel can be divided into two categories, namely petalling and shear plugging. Petalling occurs when the tip of the projectile comes into contact with the plate and initiates a crack and then few radial cracks emerge randomly from this initial crack and propagate towards the edges of the plate while the bullet penetrates through the plate resulting in a petal like deformation. Whereas shear plugging results in the ejection of a large shear plug which is usually the size of the outer diameter of the projectile with no radial crack present.

Petalling is a mixed mode fracture involving both mode I (opening mode) and mode III (out of plane shearing mode) along with a large out of plane deformation. Shear plugging on the other hand is a mode II fracture (in plane shear mode) where the

shear plane is perpendicular to the plate plane and has a more localized deformation around the area where the shear plug is sheared off.

In this study, the Navy's definition of penetration is adopted. Based on this definition a complete penetration is achieved only when the projectile completely passes through the plate onto the other side.

5.3 Pointed nose projectile

5.3.1 Pointed nose projectile on blank 4340 steel plate

Simulations were carried out by assigning an initial or impact velocity to the projectile ranging from 270 to 450 and the projectile's residual velocities after the impact are monitored. Results from the simulations show that the ballistic limit of the blank 4340 steel plate impacted by the pointed nose projectile is 335 m/s. That means the plate is considered to fail and the bullet is considered to penetrate only if the impact velocity is greater than or equal to 335 m/s.

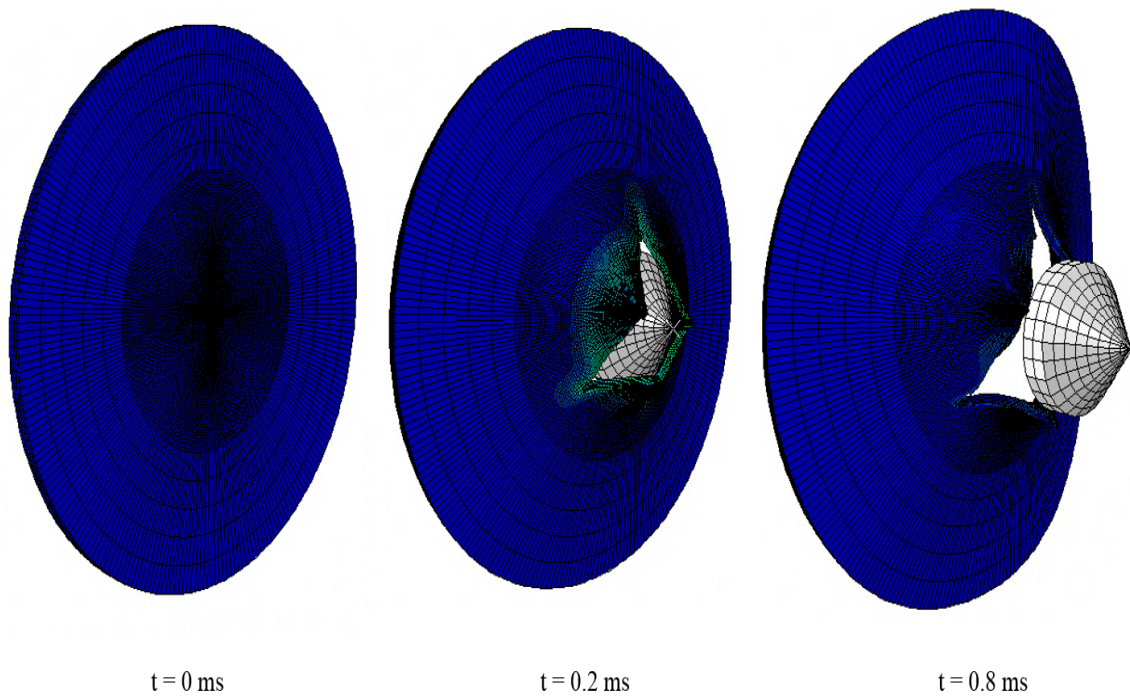


Figure 5.4: Petalling of blank 4340 plate impacted by a pointed nose projectile at a velocity of 335 m/s. Fringe plot is equivalent plastic strain, PEEQ.

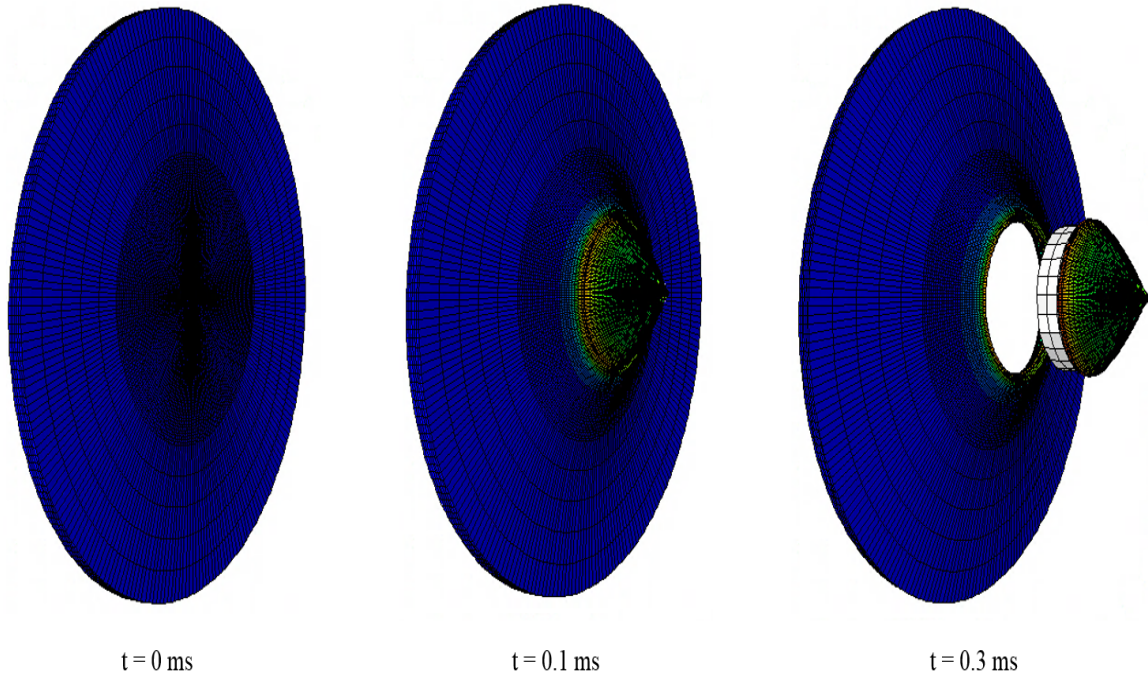


Figure 5.5: Shear plugging of blank 4340 plate impacted by a pointed nose projectile at a velocity of 430 m/s. Fringe plot is equivalent plastic strain, PEEQ.

At lower end of the velocity spectrum, it is observed that the pointed nose projectile produces petalling during penetration. Figure 5.4 shows the petalling of the blank plate when impacted by the pointed nose projectile at a velocity of 335 m/s. On the upper end of the velocity spectrum, shear plugging is observed around velocities higher than 410 m/s. Figure 5.5 shows the shearing of the blank plate when impacted with a pointed nose projectile at 430 m/s.

Figure 5.6 and figure 5.7 show the graphs for the residual velocities of the projectile and energy absorption of the blank steel plate respectively as a function of impact velocities. It is observed that the residual velocity of the projectile is very low until 335 m/s after which the projectile penetrates through the plate causing petalling. The residual velocity of the bullet increases till 370 m/s after which there is a flattening in the growth of residual velocity and from 410 m/s the blank plate fractures through shear plugging.

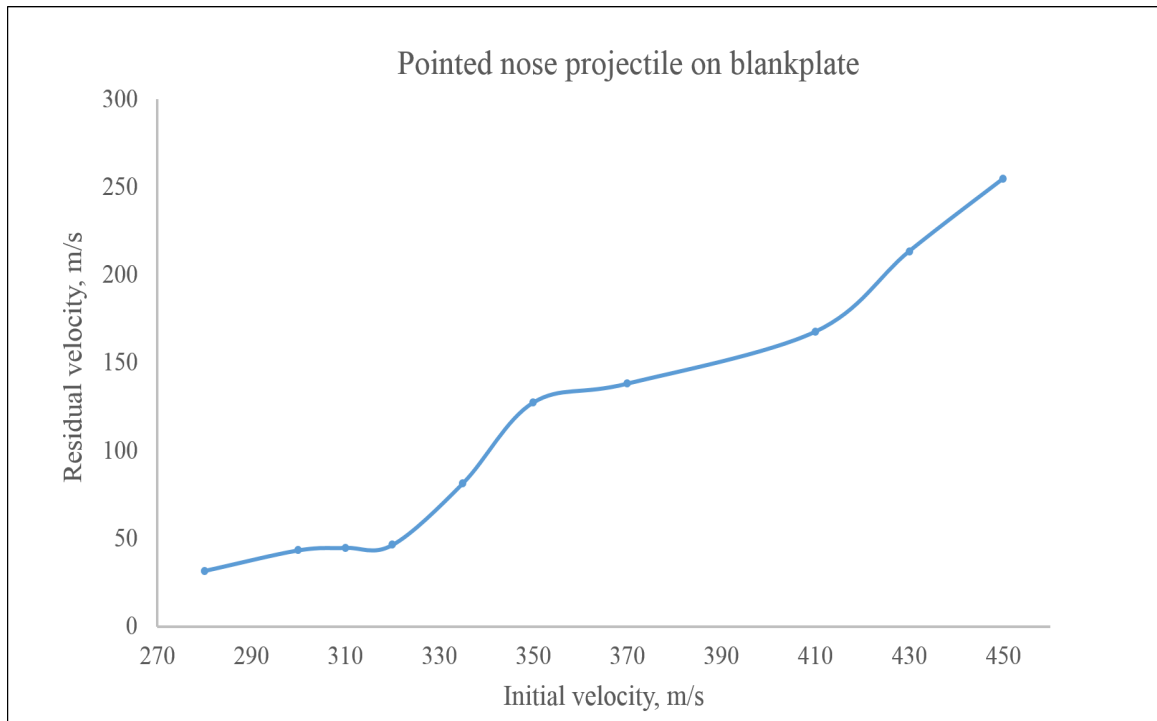


Figure 5.6: Residual velocities of pointed nose projectile after impacting blank 4340 steel plate.

The same trend can be seen in the energy absorption of the blank plate where the energy absorbed is high till 335 m/s after which the plate fails and greatly reduces its capability to absorb energy. But from 370 m/s to 410 m/s there is a slight flattening in the energy absorption when the shear plugging starts, this is speculated to be due to the fact that at high velocities, the material fails through mode II fracture where adiabatic shear bands are formed and need more energy for their propagation and failure [21]. This is the reason behind the flattening of the energy absorption during the fracture mode transition from mode I/III to mode II.

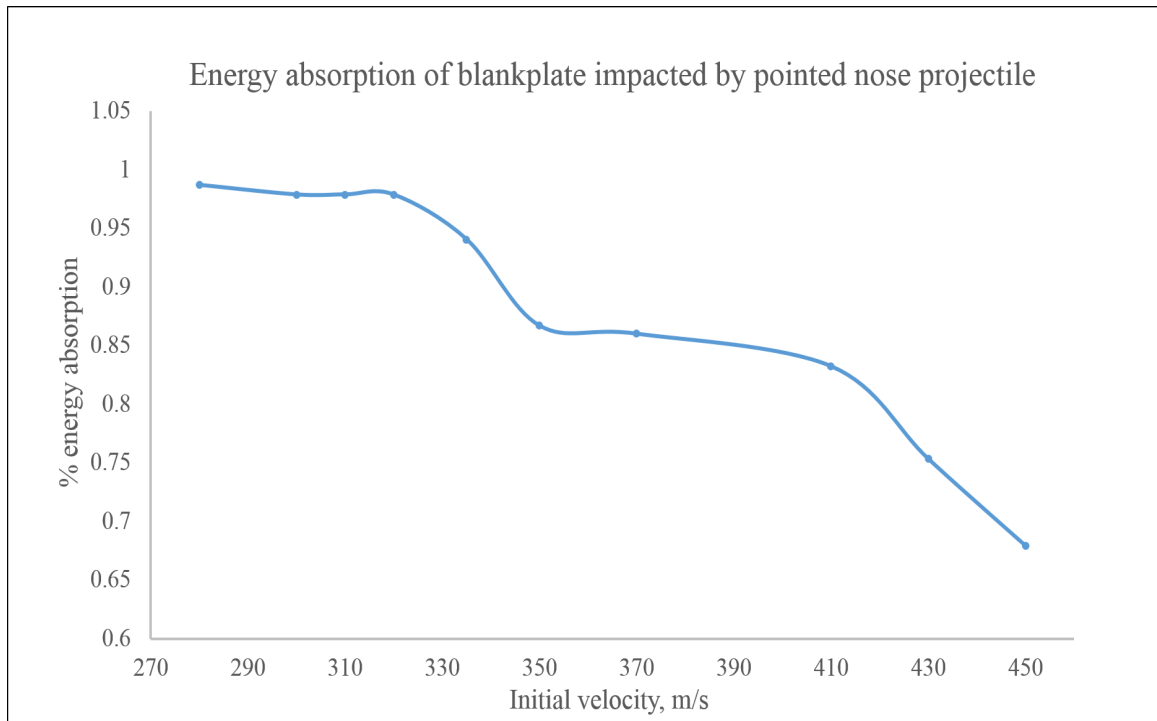


Figure 5.7: Energy absorption of the blank 4340 steel plate impacted by pointed nose projectile.

5.3.2 Comparing the residual velocities and energy absorption of blank plate, polyurea backed, polyurea sandwiched and polyurea front plates impacted by pointed nose projectile

Different scenarios were simulated during this study to determine the best scenario for the application of polyurea coating on the 4340 steel plate to improve its energy absorption capability. Figure 5.8 shows the plots of residual velocities and figure 5.9 shows the energy absorption rate of the four different scenarios namely blank plate, polyurea backed steel plate, polyurea sandwiched between two steel plates and polyurea coating on the front side or the impact side of the plate. It is observed that the polyurea coated on the backside of the plate yields better energy absorption when compared to the other models. Polyurea sandwiched between the plates or polyurea at the front did not show any impact on the penetration resistance.

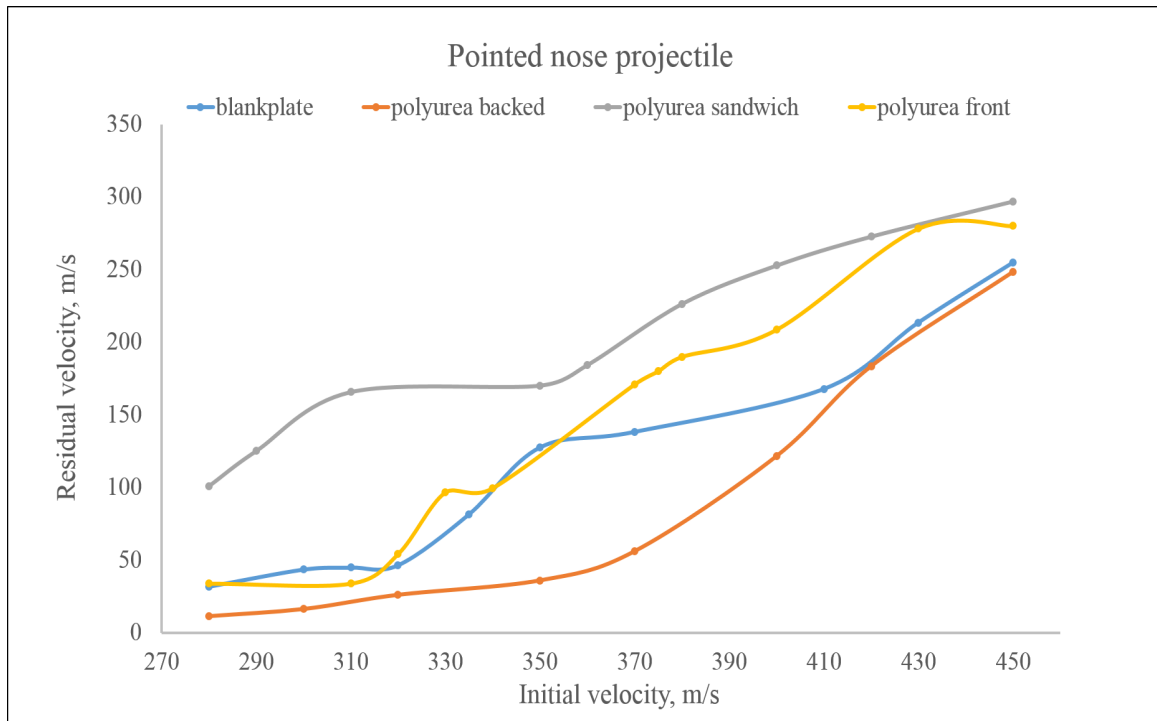


Figure 5.8: Residual velocities of pointed nose projectile impacting blank plate, polyurea backed, polyurea sandwiched and polyurea front plates.

5.3.3 Best energy absorption for pointed nose projectile

From section 5.3.2 it is observed that the polyurea backed 4340 steel plate offers the highest penetration resistance to the pointed nose projectile by its ability in stretching after the impact and by absorbing and dissipating more energy through this. The polyurea stretches to its maximum limit until the projectile completely pierces through the steel plate and ruptures the polyurea as well. It can be seen from figure 5.10 that the ballistic limit of the 4340 steel is increased by 10% from 335 m/s to 370 m/s by applying the polyurea on to the backside of the plate and the shaded region in the figure 5.11 represents the additional energy absorbed by the polyurea from the projectile.

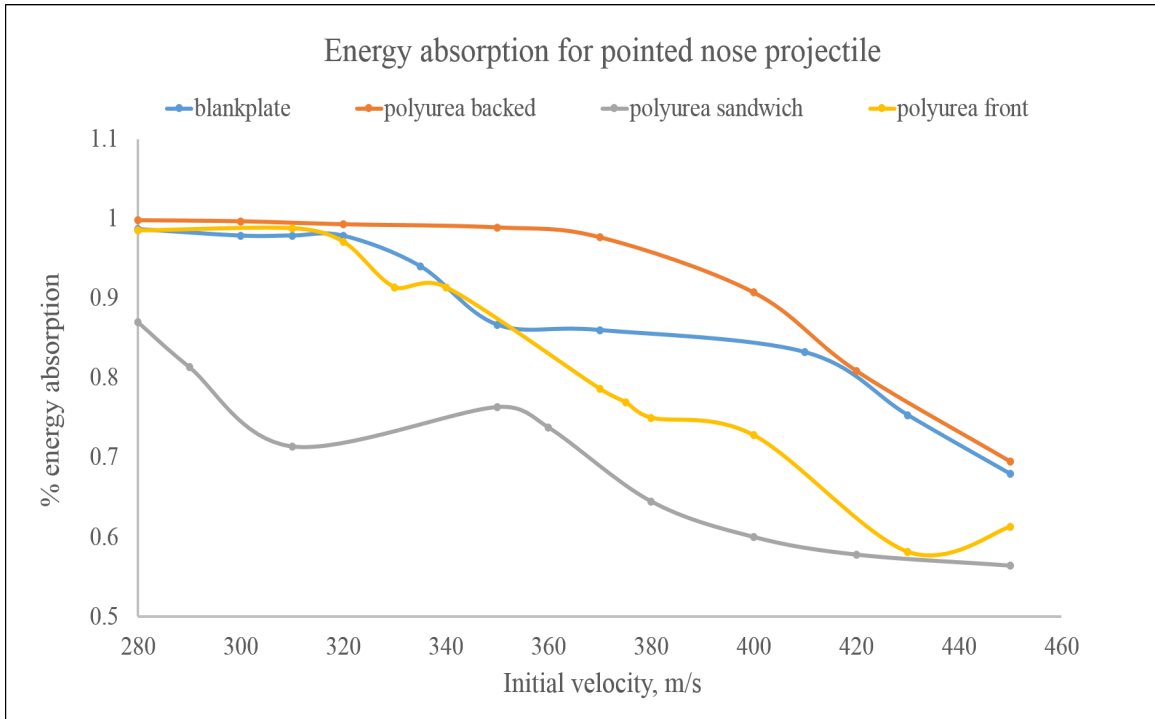


Figure 5.9: Energy absorption of blank plate, polyurea backed, polyurea sandwiched and polyurea front plates impacted by pointed nose projectile.

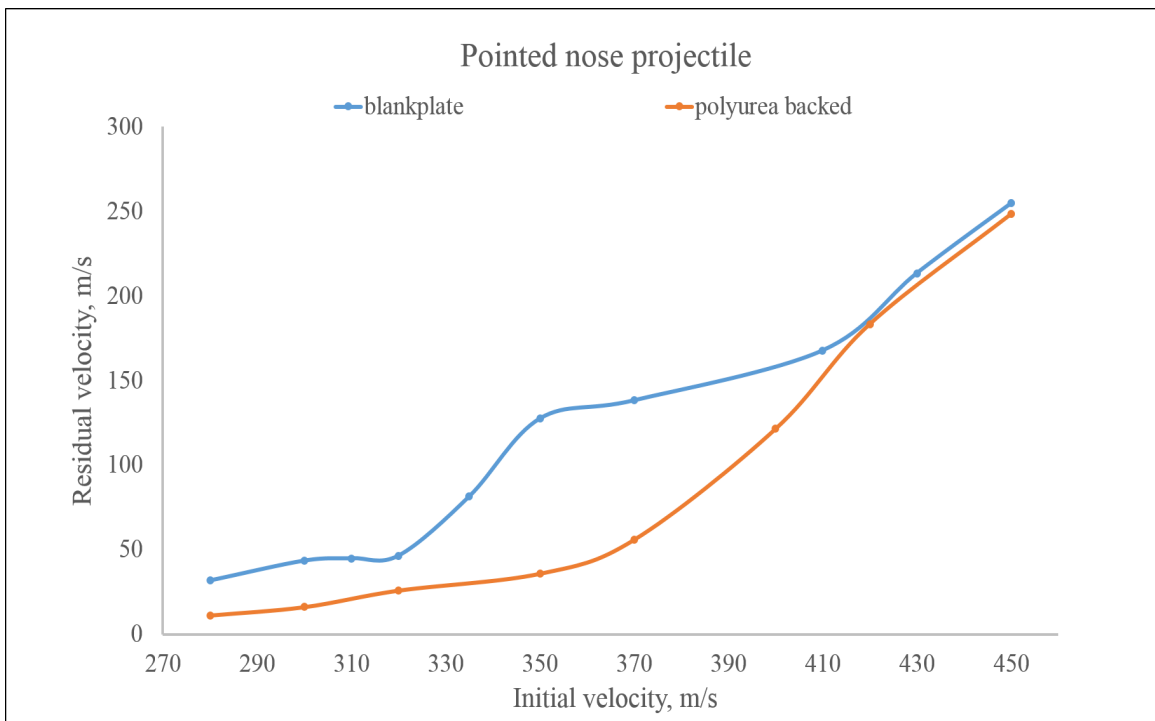


Figure 5.10: Residual velocities of pointed nose projectile impacting blank plate and polyurea backed steel plate.

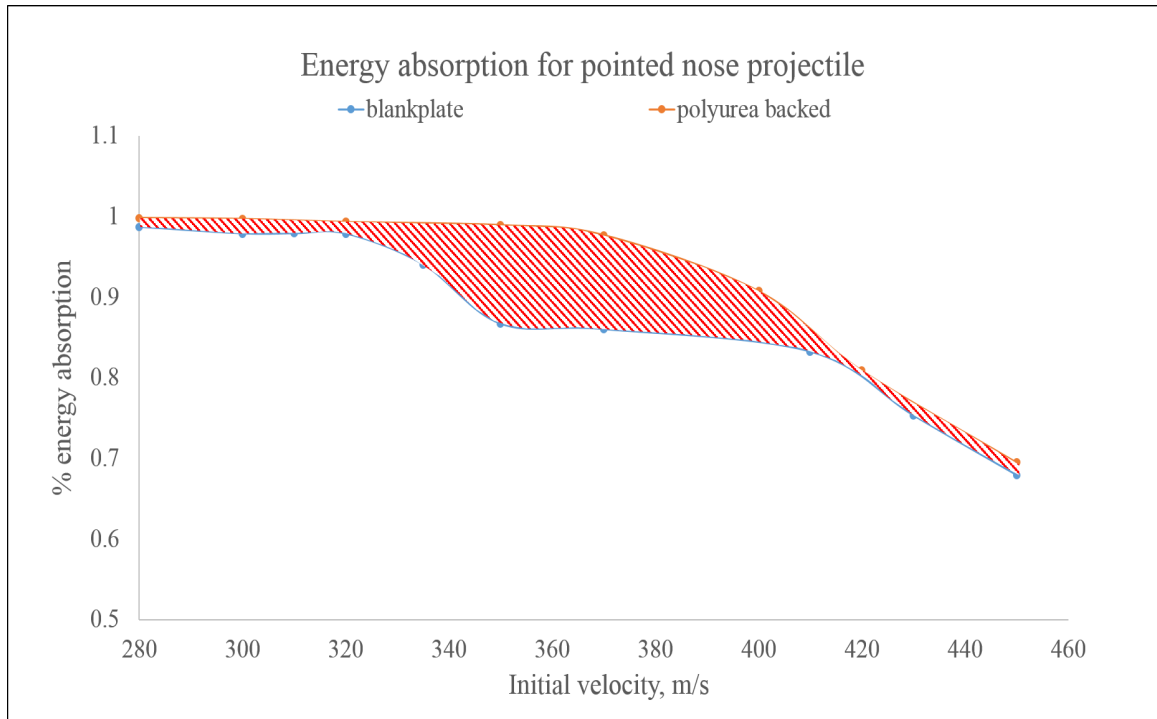


Figure 5.11: Energy absorption of blank plate and polyurea backed steel plate impacted by pointed nose projectile.

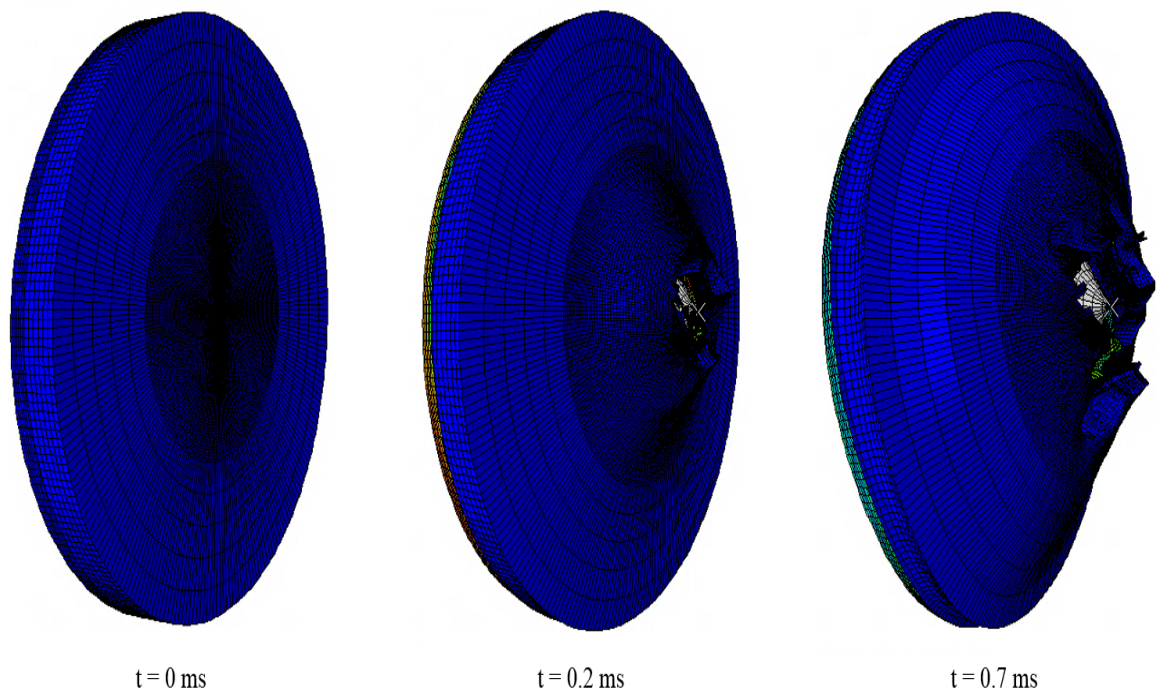


Figure 5.12: Damage progression for polyurea backed 4340 steel plate impacted by pointed nose projectile at a velocity of 360 m/s. Fringe plot is von Mises stress.

5.4 Jacket nose projectile

5.4.1 Jacket nose projectile on blank 4340 steel plate

Results from the simulations showed that the ballistic limit for the blank 4340 steel plate when impacted by the jacket nose projectile is 380 m/s after which the material fails. Due to the unusual shape of the projectile, the ballistic limit of the plate is effected. At lower velocities below the ballistic limit there seems to be shearing of a small plug even though the projectile does not completely penetrate the plate and there seems to be insignificant trace of petalling. As seen in figure 5.13, the residual velocity increases after 380 m/s and in figure 5.14 the energy absorption of the blank plate is high until 380 m/s after which its starts dropping down.

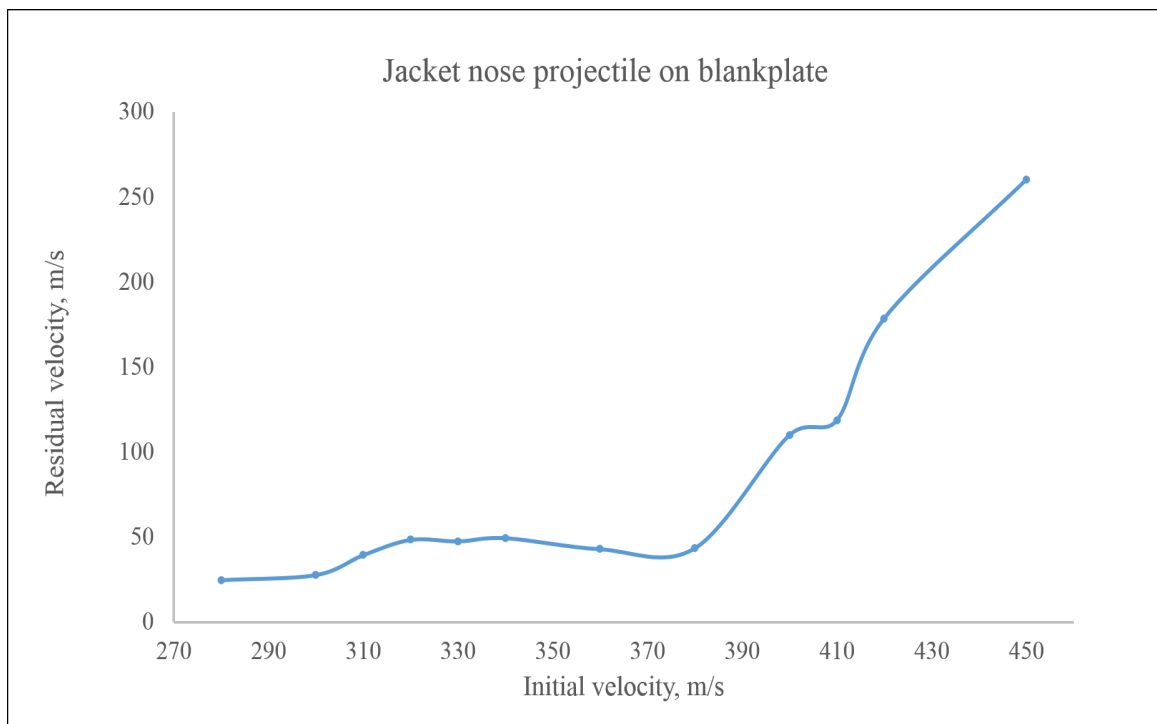


Figure 5.13: Residual velocities of jacket nose projectile after impacting blank 4340 steel plate

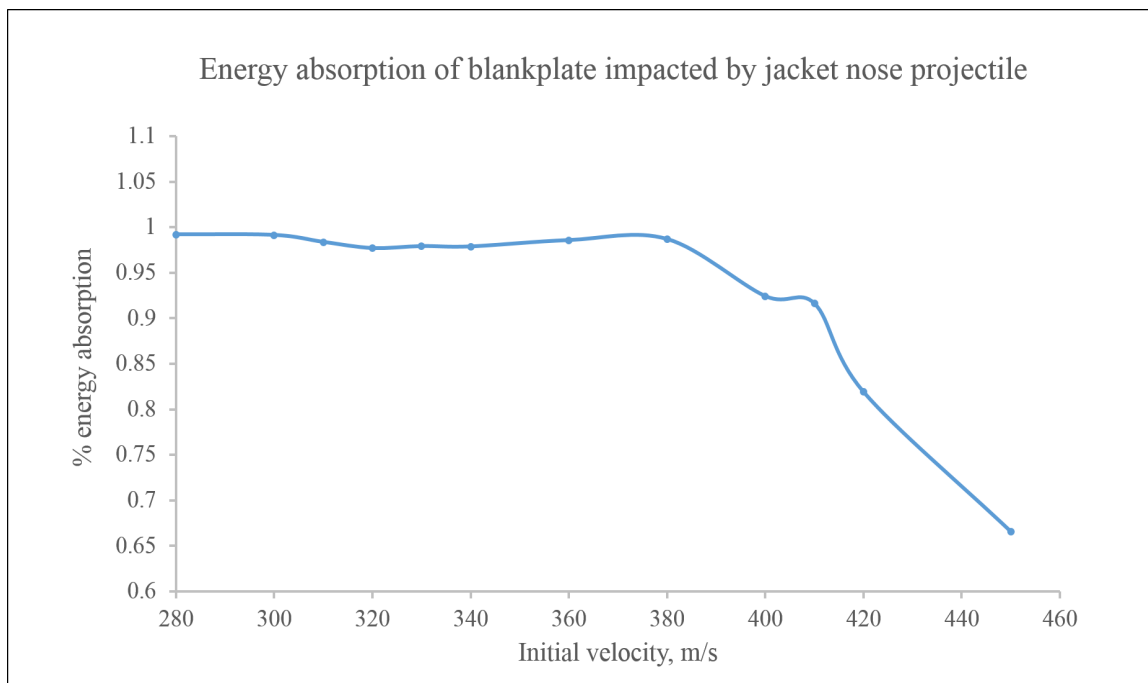


Figure 5.14: Energy absorption of blank 4340 steel plate after impacted by jacket nose projectile.

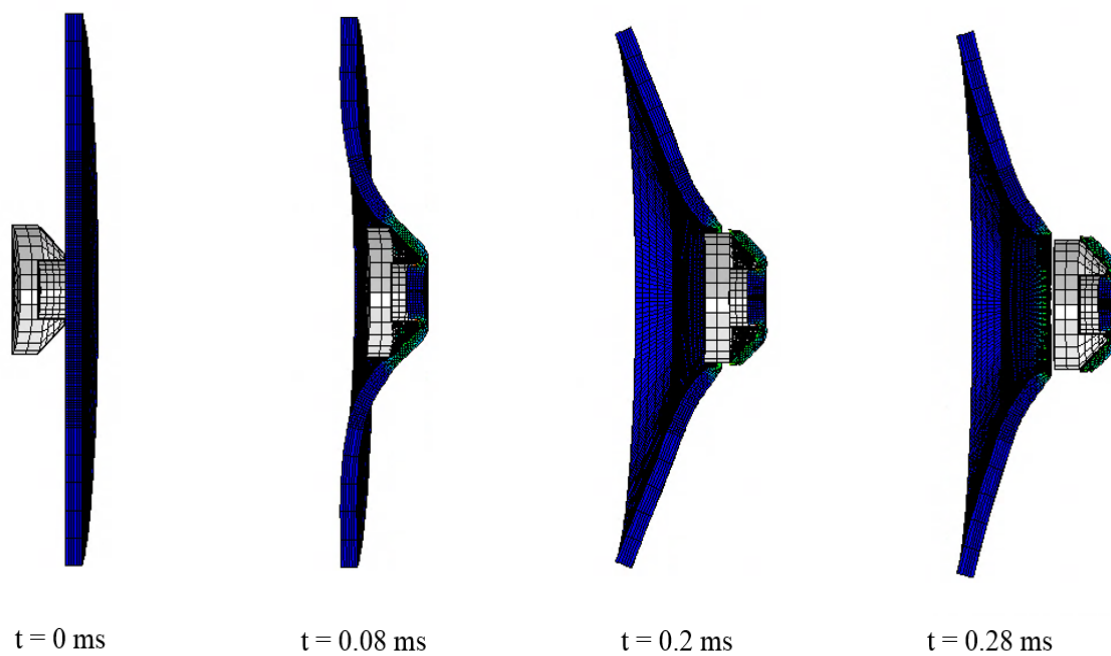


Figure 5.15: Shear plugging of blank 4340 plate impacted by a jacket nose projectile at a velocity of 410 m/s. Fringe plot is equivalent plastic strain, PEEQ.

5.4.2 Comparing the residual velocities and energy absorption of blank plate, polyurea backed, polyurea sandwiched and polyurea front plates with jacket nose projectile

All four scenarios mentioned above are simulated and the results obtained are shown in the figure 5.16 and figure 5.17. The polyurea sandwiched steel plate configuration gives the lowest energy absorption while the polyurea coated at the front gives the highest energy absorption for the jacket nose projectile. It is also observed that polyurea backed plate shows a penetration resistance similar to blank plate.

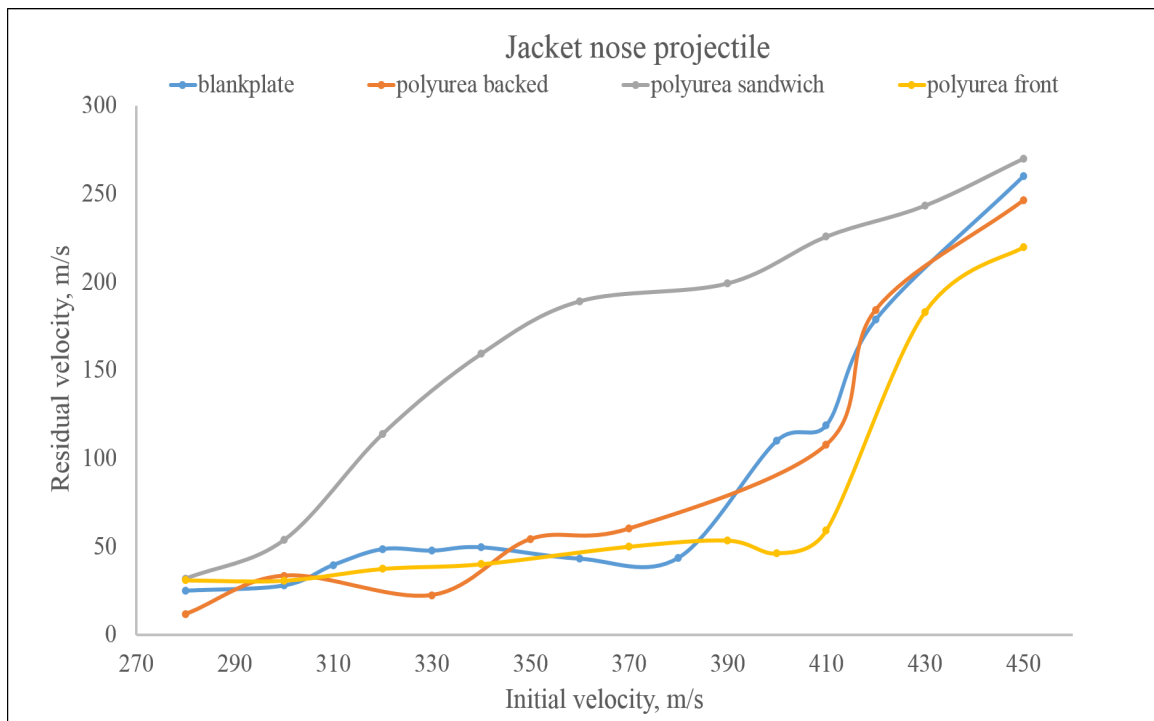


Figure 5.16: Residual velocities of jacket nose projectile impacting blank plate, polyurea backed, polyurea sandwiched and polyurea front plates.

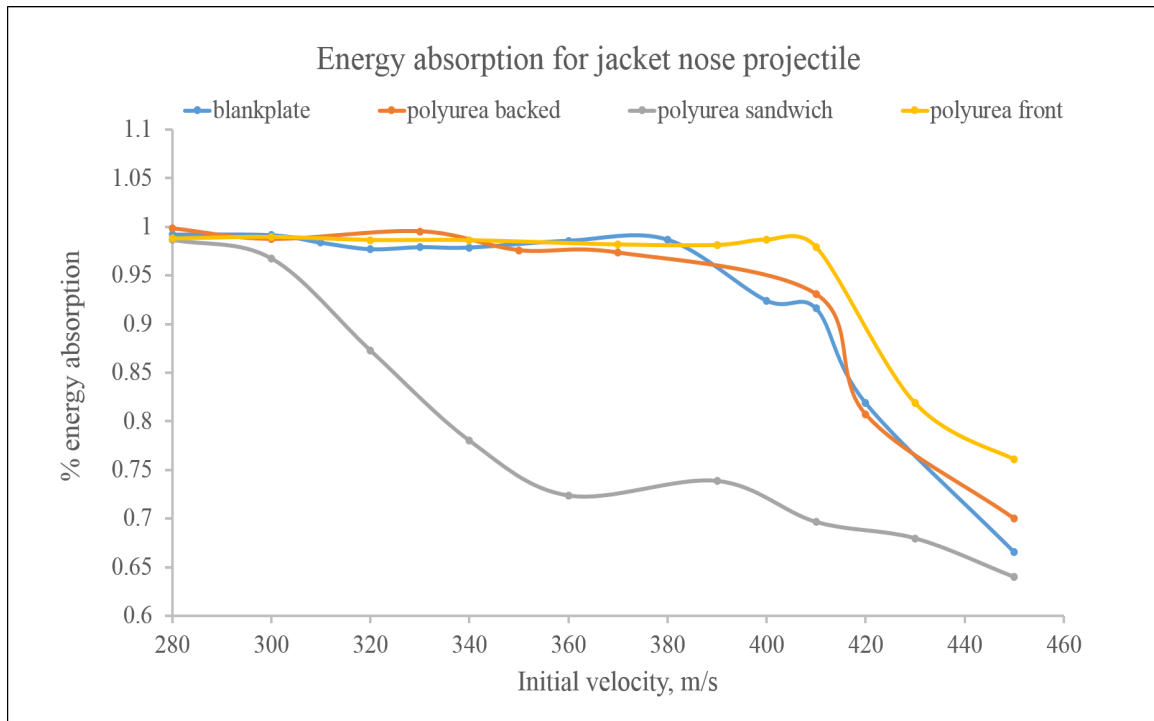


Figure 5.17: Energy absorption of blank plate, polyurea backed, polyurea sandwiched and polyurea front plates impacted by jacket nose projectile

5.4.3 Best energy absorption for jacket nose projectile

Based on the four scenarios of the jacket nose projectile, it is observed that polyurea coated at front side of the plate has been the best configuration to maximize the penetration resistance of the plate increasing the ballistic limit of the plate by 11% from 370 m/s to 410 m/s as shown in figure 5.18. Also the shaded region depicted in figure 5.19 shows the increase in the amount of energy dissipated by polyurea upon impact by jacket nose projectile. Figure 5.20 shows the energy dissipation by the polyurea and the penetration resistance of steel even though a small plug is ejected from the plate

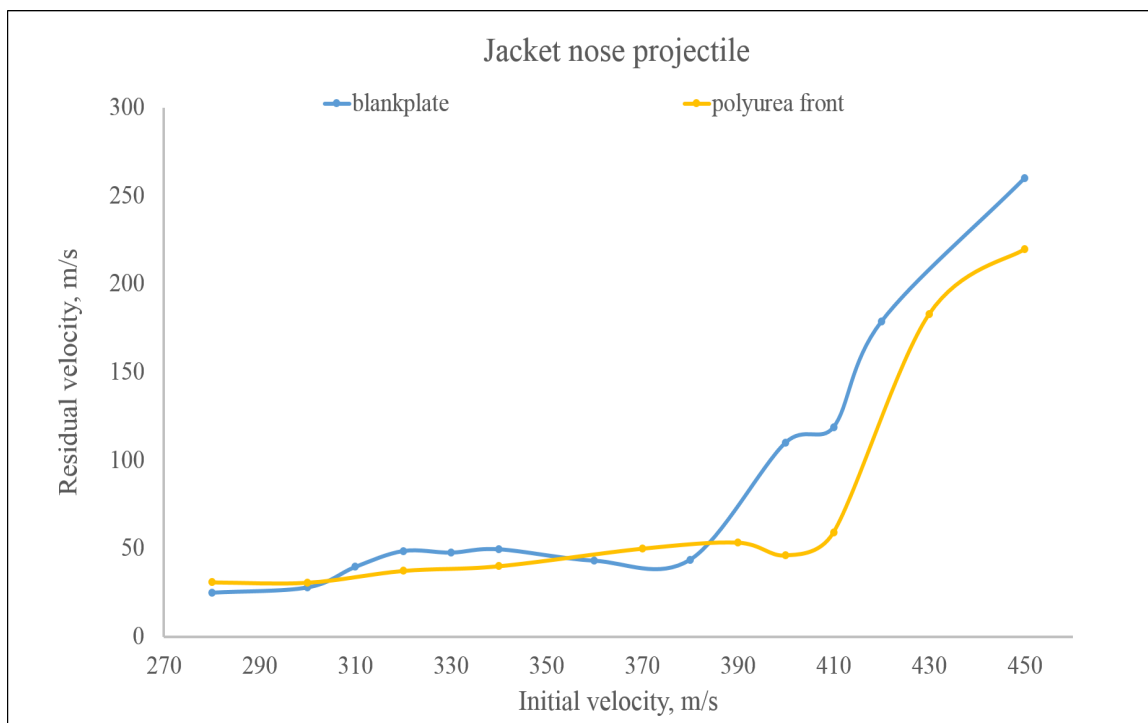


Figure 5.18: Residual velocities of jacket nose projectile impacting blank plate and polyurea backed steel plate.

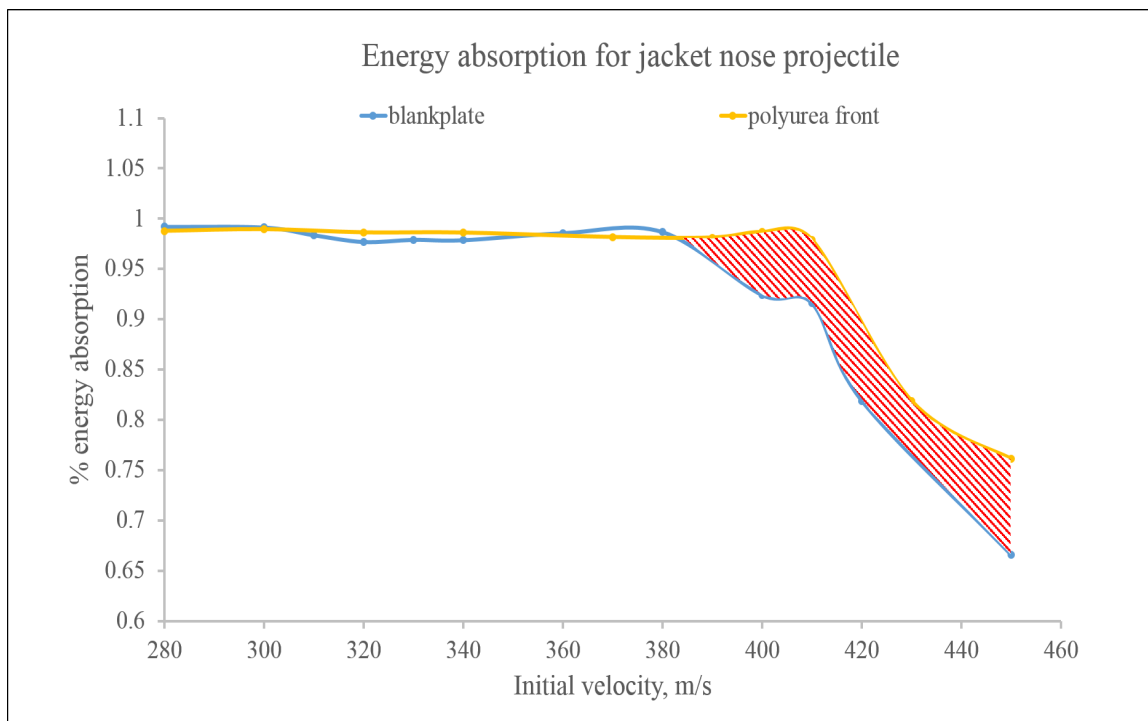


Figure 5.19: Energy absorption of blank plate and polyurea backed steel plate impacted by jacket nose projectile.

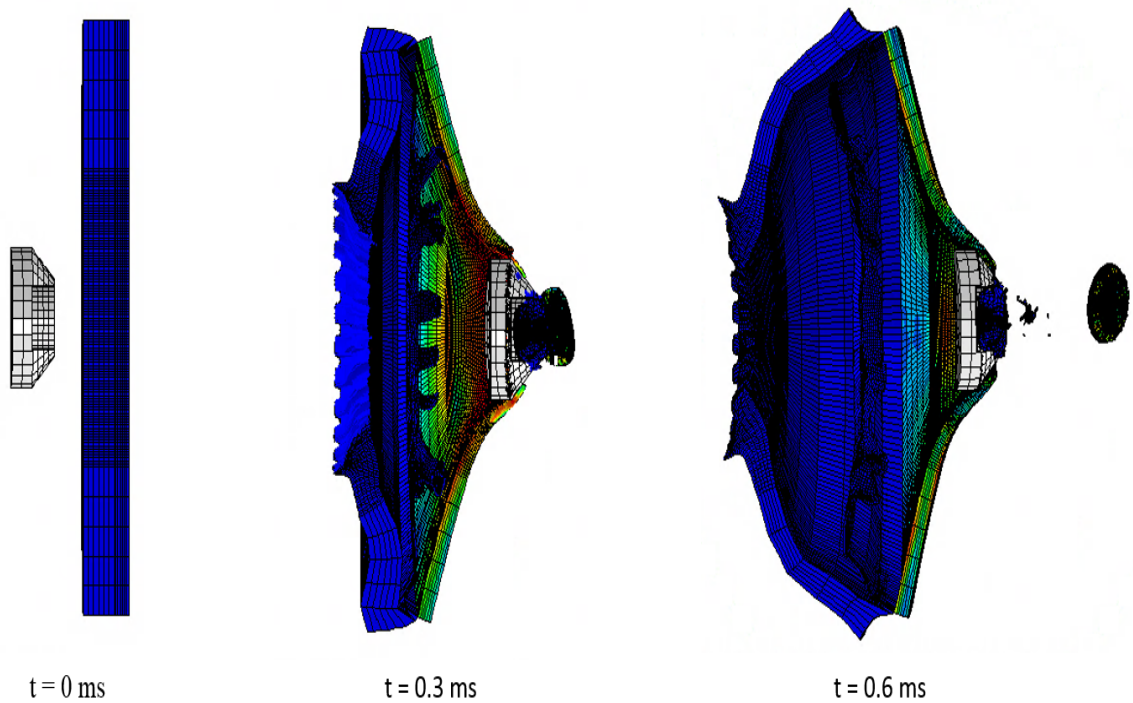


Figure 5.20: Damage progression for polyurea backed 4340 steel plate impacted by jacket nose projectile at a velocity of 360 m/s. Fringe plot is von Mises stress.

5.5 Round nose projectile

5.5.1 Round nose projectile on blank 4340 steel plate

As shown in figure 5.21, simulations of round nose bullet impacting a blank 4340 steel plate revealed the ballistic limit of the plate to be 340 m/s after which the round nose penetrates the plate ejecting a large shear plug. At no point of time in the velocity range does the round nose display petalling not even a small trace like in the case of jacket nose, this may be due to the spherical shape of the bullet. Even the energy absorption curve from the figure 5.22 shows a smooth decline after the ballistic limit is reached. Figure 5.23 shows the damage progression and ejection of a shear plug when the blank plate is impacted by the round nose projectile at 360 m/s.

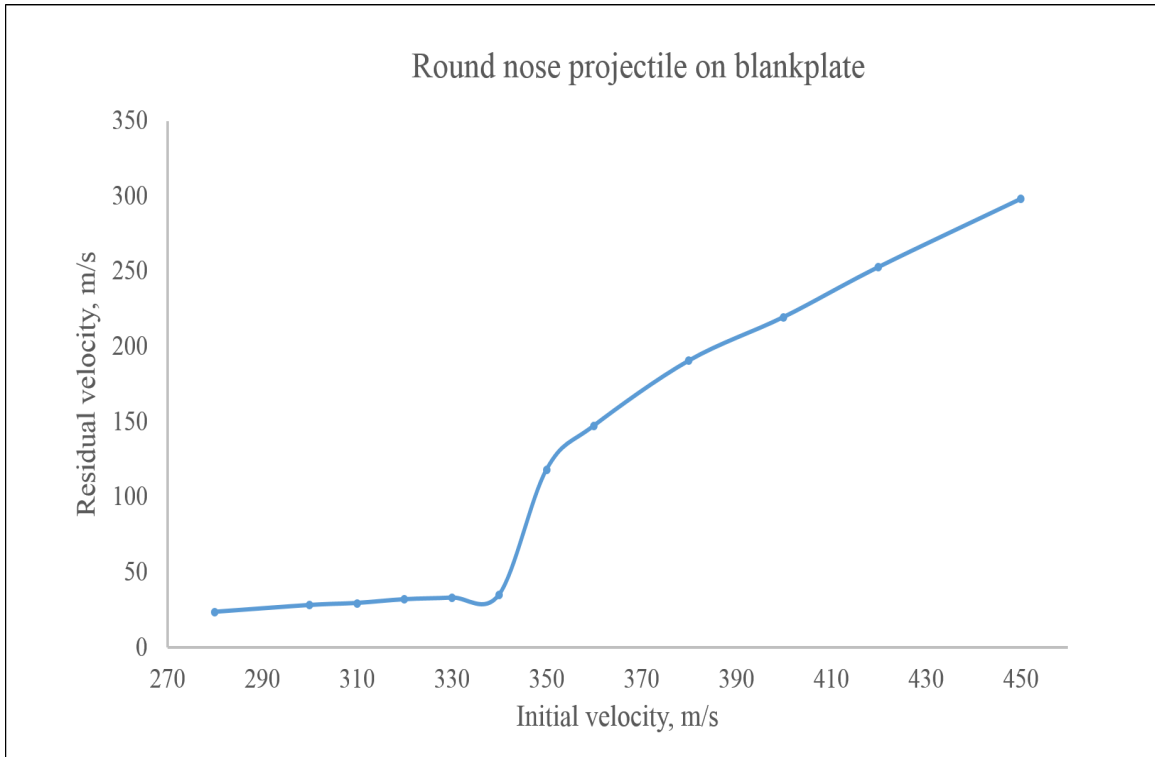


Figure 5.21: Residual velocities of round nose projectile after impacting blank 4340 steel plate

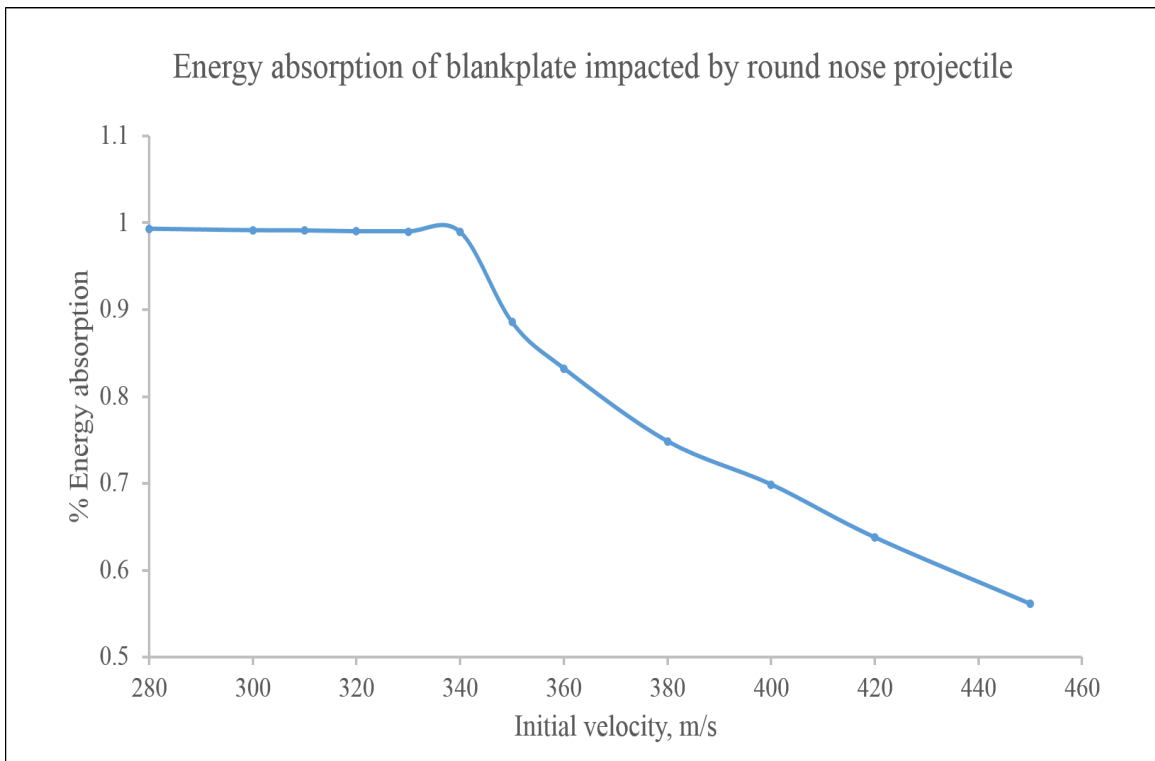


Figure 5.22: Energy absorption of blank 4340 steel plate impacted by round nose projectile.

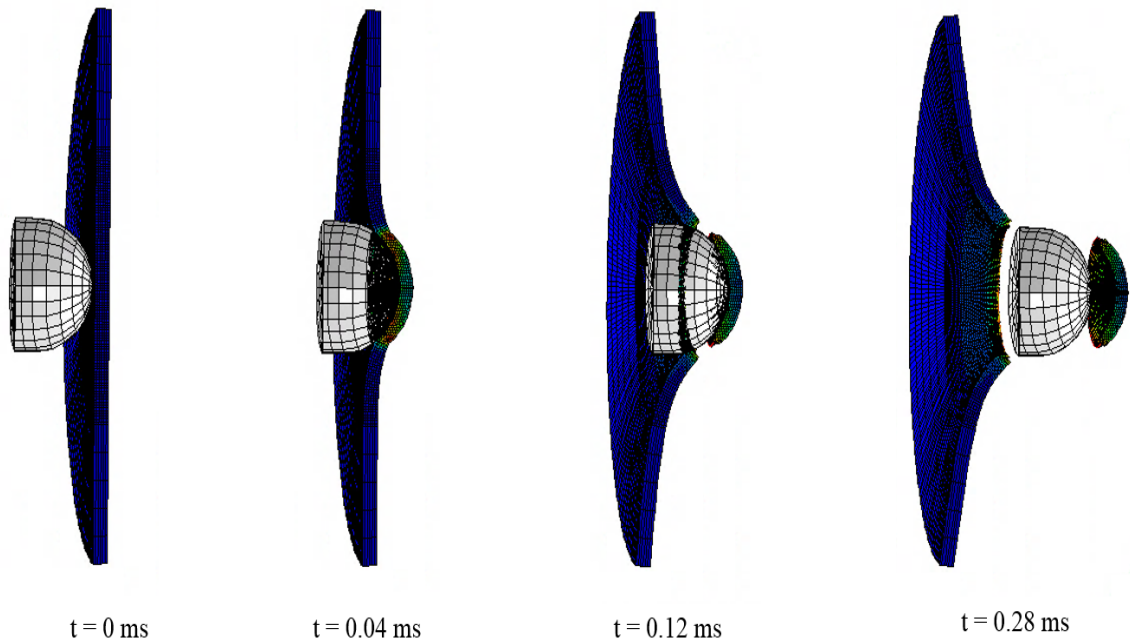


Figure 5.23: Shear plugging of blank 4340 plate impacted by round nose projectile at a velocity of 360 m/s. Fringe plot is equivalent plastic strain, PEEQ.

5.5.2 Comparing the residual velocities and energy absorption of blank plate, polyurea backed, polyurea sandwiched and polyurea front plates with round nose projectile

When the round nose is impacted with different scenarios in this study, it is found that except for polyurea sandwiched configuration, the other two helped the blank plate to increase its penetration resistance as shown in figure 5.24. All the energy absorption curves have been seen smoothly declining except for polyurea sandwich which shows a flattening trend at 360 m/s due to its failure transition from petalling to shear plugging as shown in figure 5.25. This change in the polyurea sandwich may be attributed to the fact that the petalling occurs in the second plate on the back because of the shear plug from the first plate carried along by the round nose projectile.

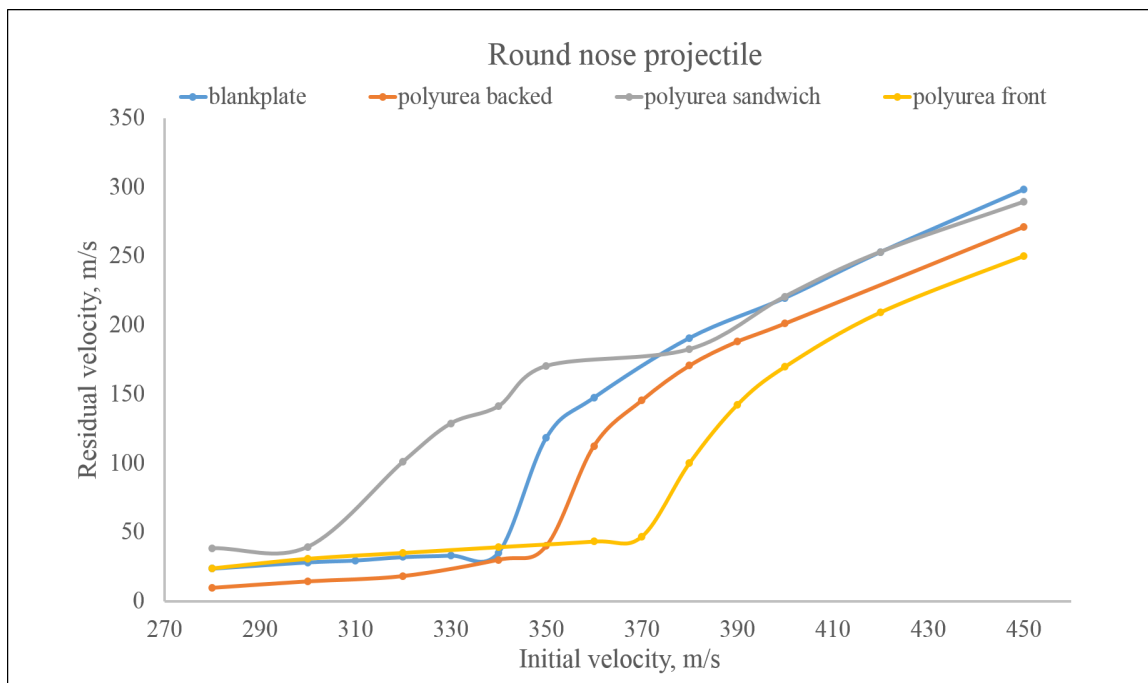


Figure 5.24: Residual velocities of round nose projectile impacting blank plate, polyurea backed, polyurea sandwiched and polyurea front plates.

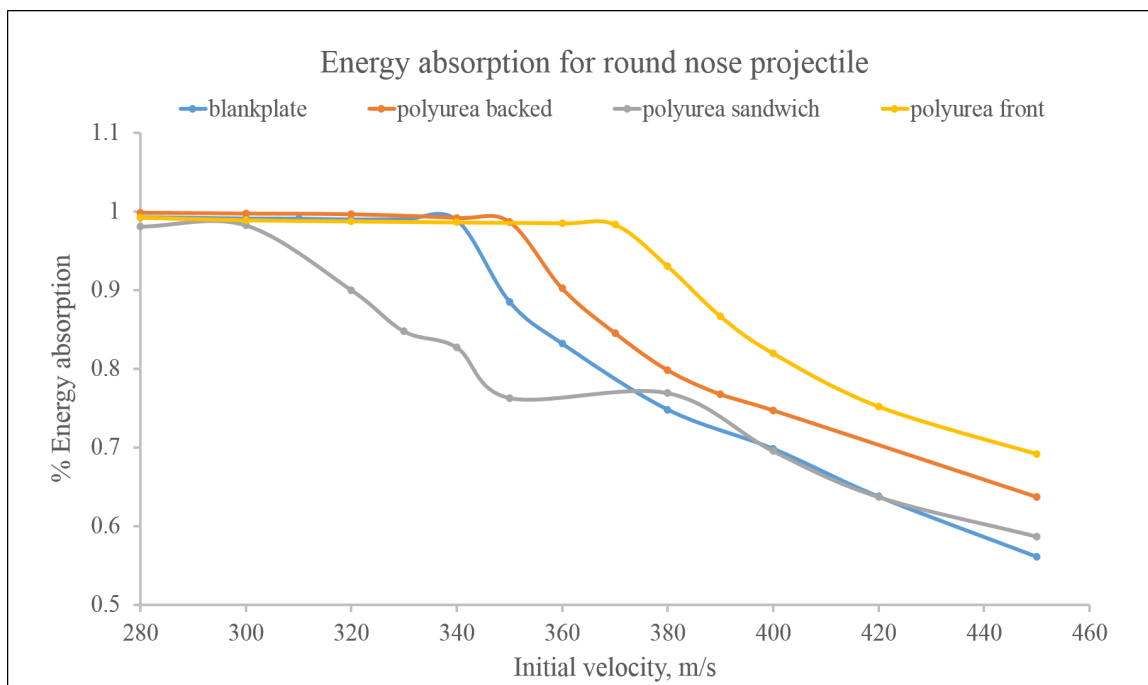


Figure 5.25: Energy absorption of blank plate, polyurea backed, polyurea sandwiched and polyurea front plates impacted by round nose projectile

5.5.3 Best energy absorption for round nose projectile

Of all the configurations simulated with the round nose projectile, polyurea coated at the front side of the plate taking the initial impact delayed the penetration by 30 m/s as shown in figure 5.26. Also the shaded region in figure 5.27 shows the additional kinetic energy absorbed by the polyurea when added to the impact side of the plate. Figure 5.28 shows the progression of the polyurea and the steel plate upon impact by round nose projectile at a velocity of 360 m/s. It is seen that the polyurea upon impact absorbs part of the projectile's kinetic energy there by reducing its speed to below the ballistic limit.

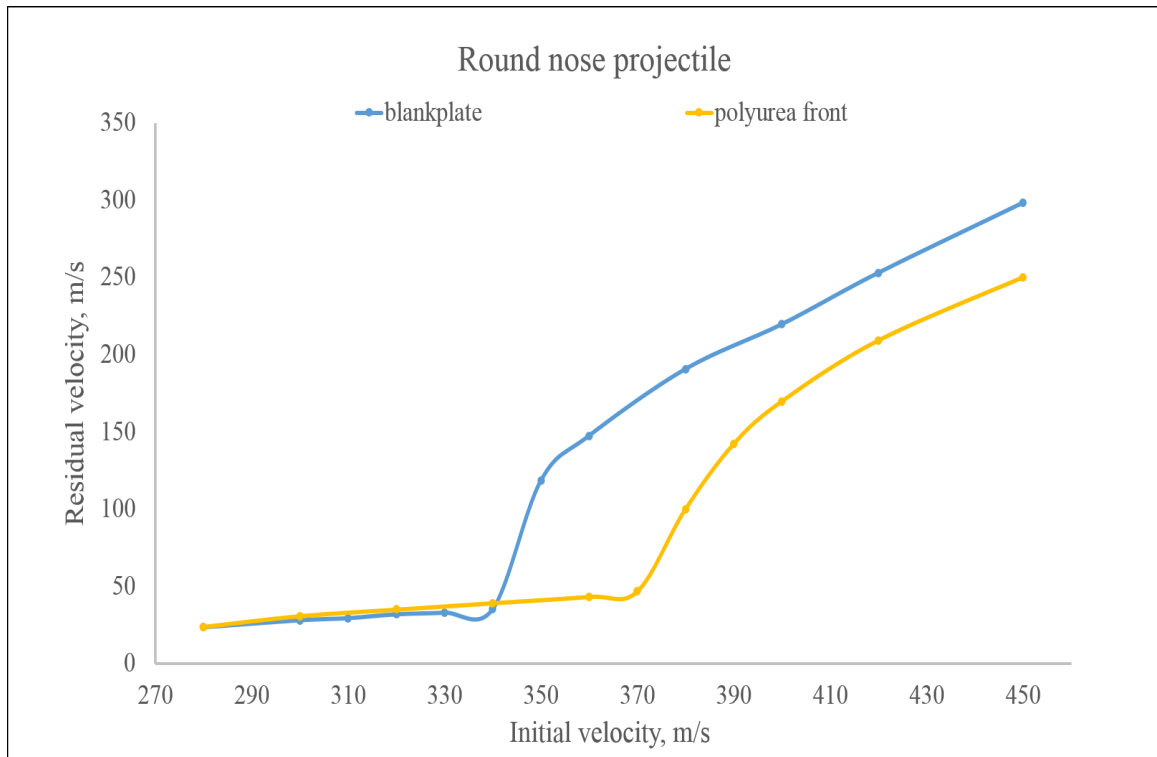


Figure 5.26: Residual velocities of round nose projectile impacting blank plate and polyurea backed steel plate.

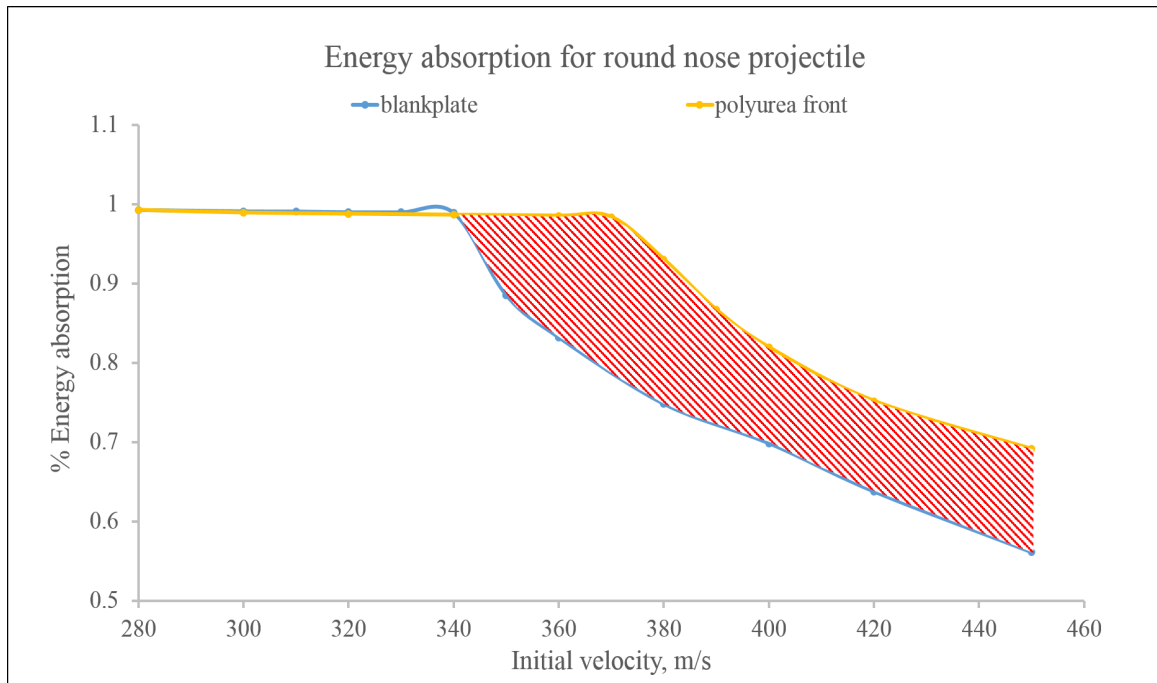


Figure 5.27: Energy absorption of blank plate and polyurea backed steel plate impacted by round nose projectile

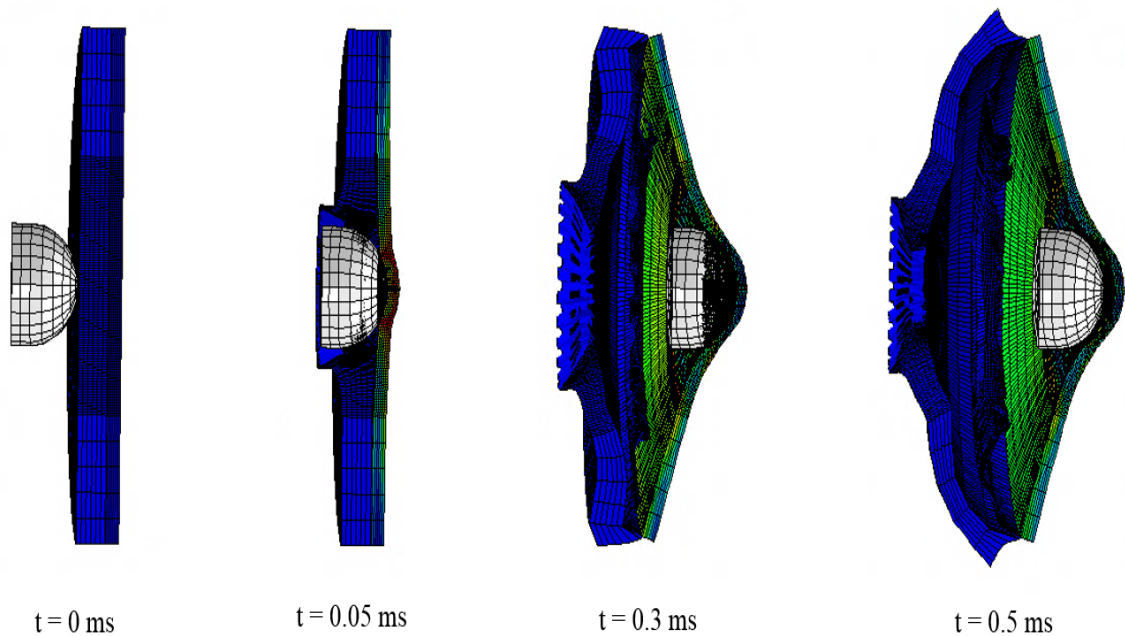


Figure 5.28: Damage progression for polyurea backed 4340 steel plate impacted by round nose projectile at a velocity of 360 m/s. Fringe plot is von Mises stress.

5.6 Flat nose projectile

5.6.1 Flat nose projectile on blank 4340 steel plate

Upon impacting the flat nose projectile on to the blank 4340 steel plate with a wide range of velocities it is observed from figure 5.29 that the plate can resist the penetration only till 330 m/s after which the plate fails by shear plugging with a hint of petalling at the rim formed from shearing. From figure 5.30 it can be observed that the energy absorption is high until the impact velocity reaches 330 m/s after which it starts to decline. But at 380 m/s there is a flattening in the energy absorbed due to the mode transition from the mixed I, II and III to the adiabatic shear banded mode II.

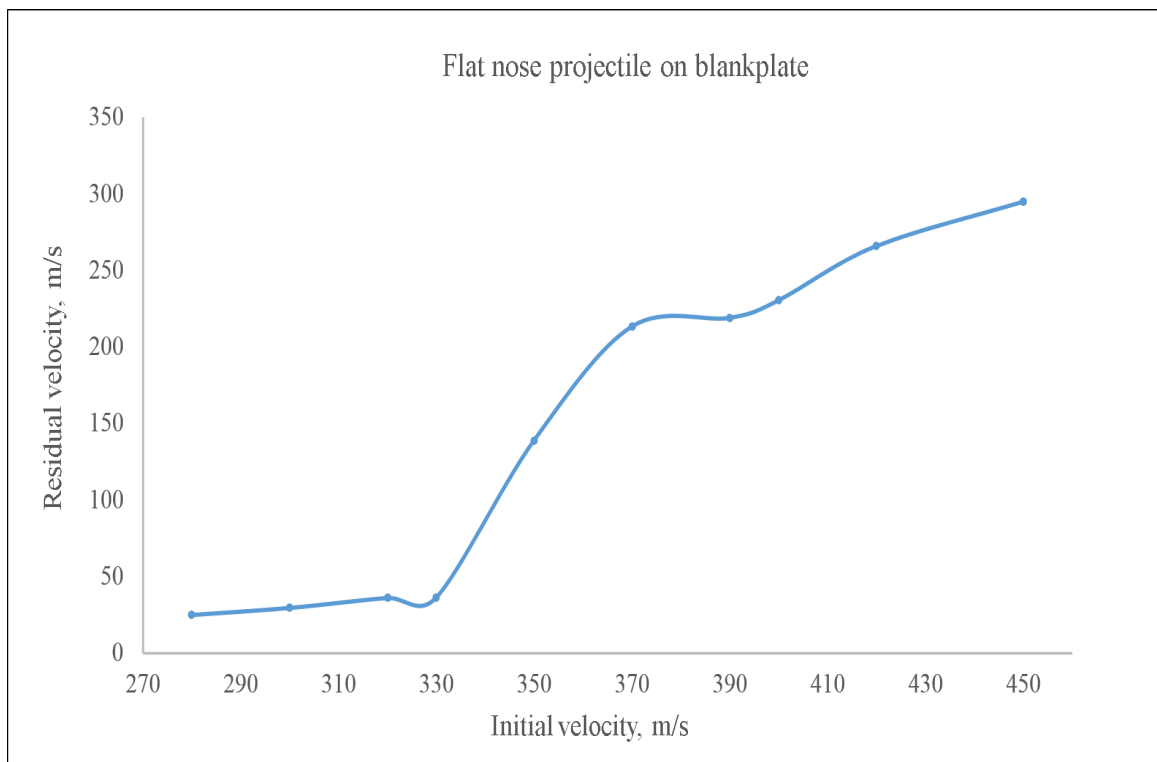


Figure 5.29: Residual velocities of flat nose projectile after impacting blank 4340 steel plate.

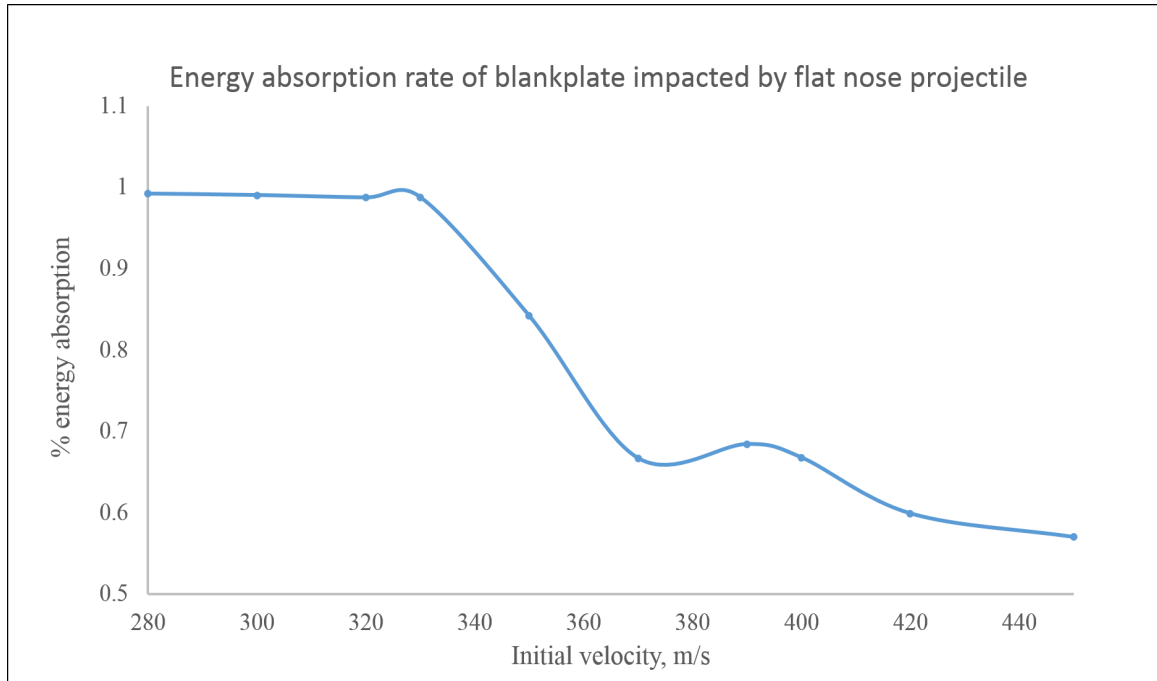


Figure 5.30: Energy absorption of blank 4340 steel plate impacted by flat nose projectile.

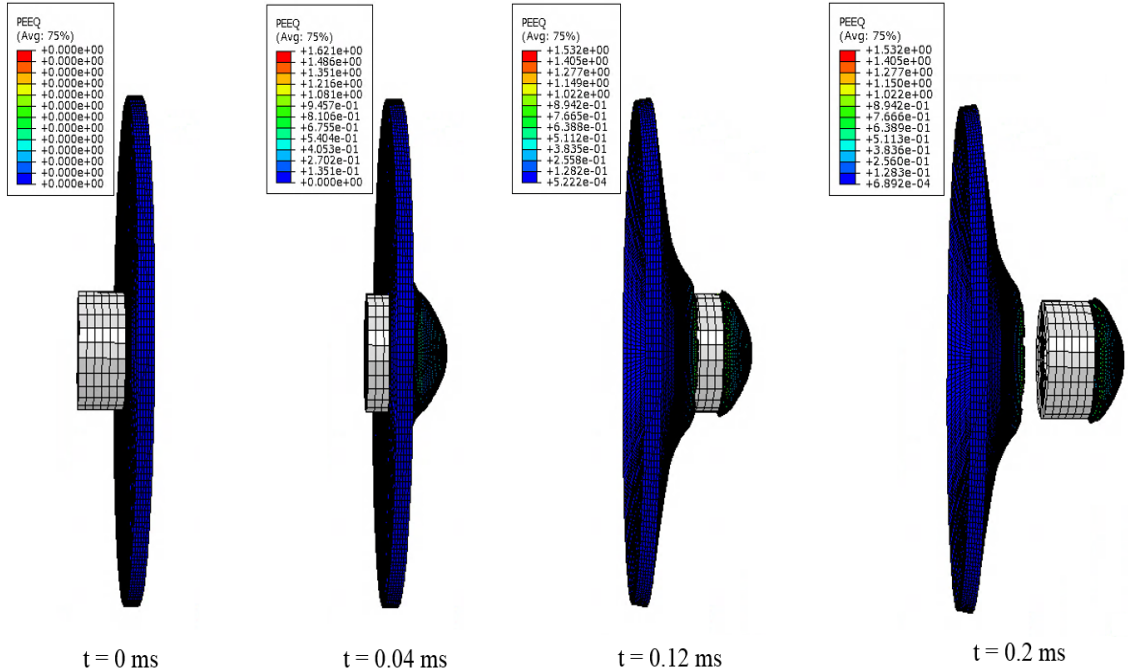


Figure 5.31: Shear plugging of blank 4340 plate impacted by flat nose projectile at a velocity of 360 m/s. Fringe plot is equivalent plastic strain, PEEQ.

5.6.2 Comparing the residual velocities and energy absorption of blank plate, polyurea backed, polyurea sandwiched and polyurea front plates with flat nose projectile

After simulating all the scenarios which include blank plate, polyurea backed, polyurea sandwiched and polyurea front, a conclusion was drawn from the figure 5.32 that all the scenarios help the blank steel plate in improving its ballistic limit and energy absorption rates in figure 5.33 as well. But the scenario of polyurea backed plate is almost similar to blank plate.

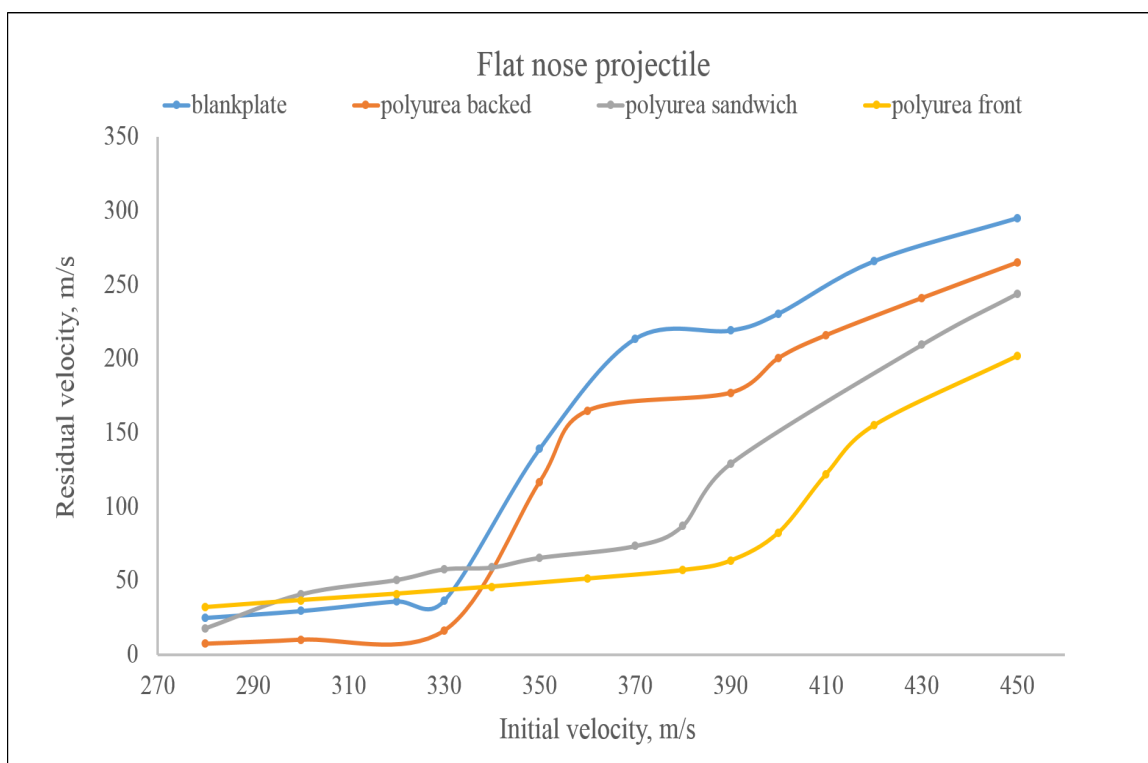


Figure 5.32: Residual velocities of flat nose projectile impacting blank plate, polyurea backed, polyurea sandwiched and polyurea front plates.

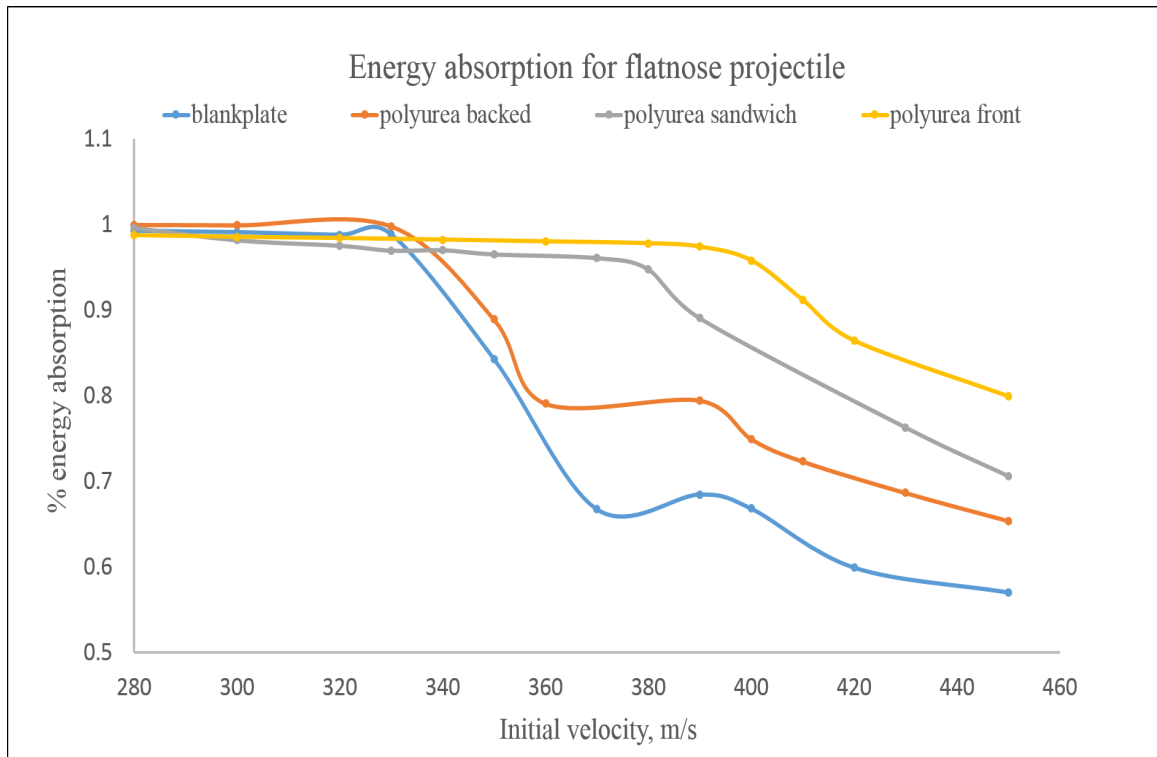


Figure 5.33: Energy absorption of blank plate, polyurea backed, polyurea sandwiched and polyurea front plates impacted by flat nose projectile

5.6.3 Best energy absorption for flat nose projectile

All though all the configurations helped the blank 4340 steel plate in improving its energy dissipation capability, polyurea coated at the front as shown in figure 5.34 improves the ballistic limit of the plate by 18% from 330 m/s to 390 m/s. As it can also be seen from the figure 5.35 that the shaded region which represents the increase in the energy absorption due to the addition of polyurea is very large, largest among all the scenarios. Figure 5.36 shows the progression of the impact and the reaction of the polyurea up on the impact.

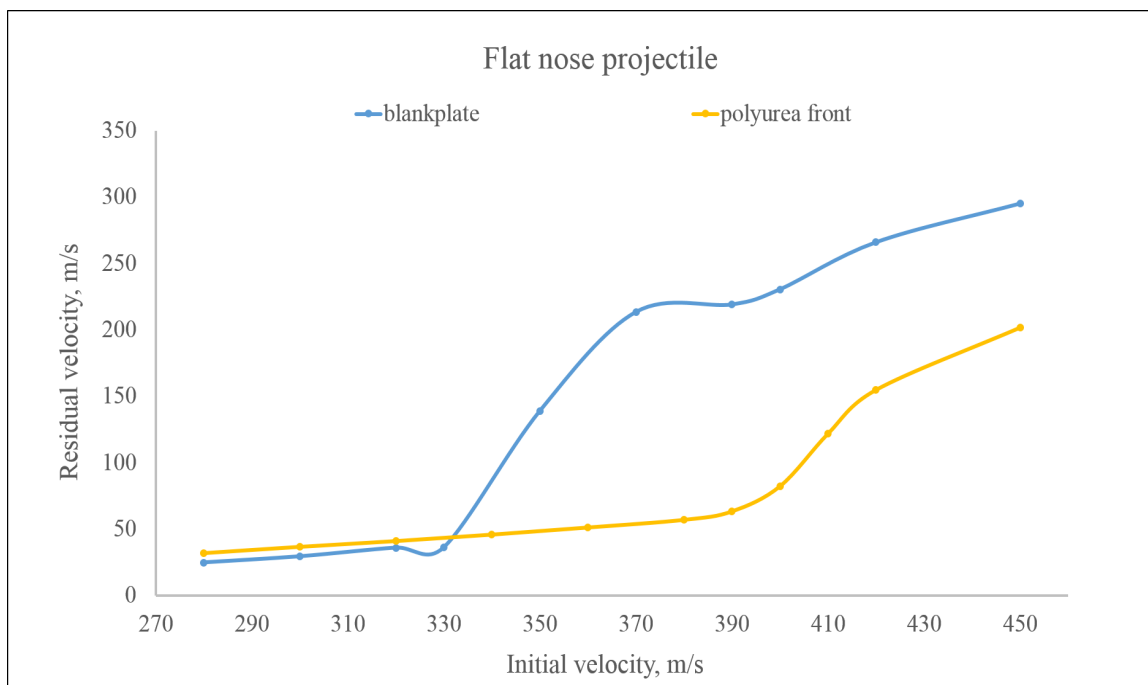


Figure 5.34: Residual velocities of flat nose projectile impacting blank plate and polyurea backed steel plate.

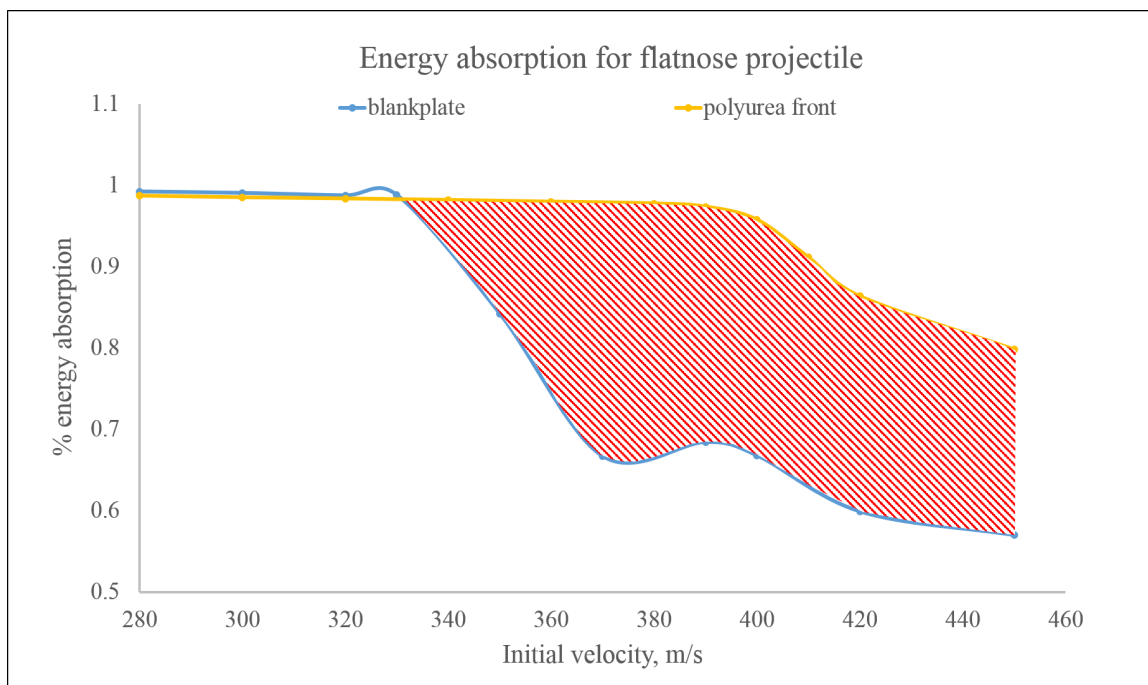


Figure 5.35: Energy absorption of blank plate and polyurea backed steel plate impacted by flat nose projectile

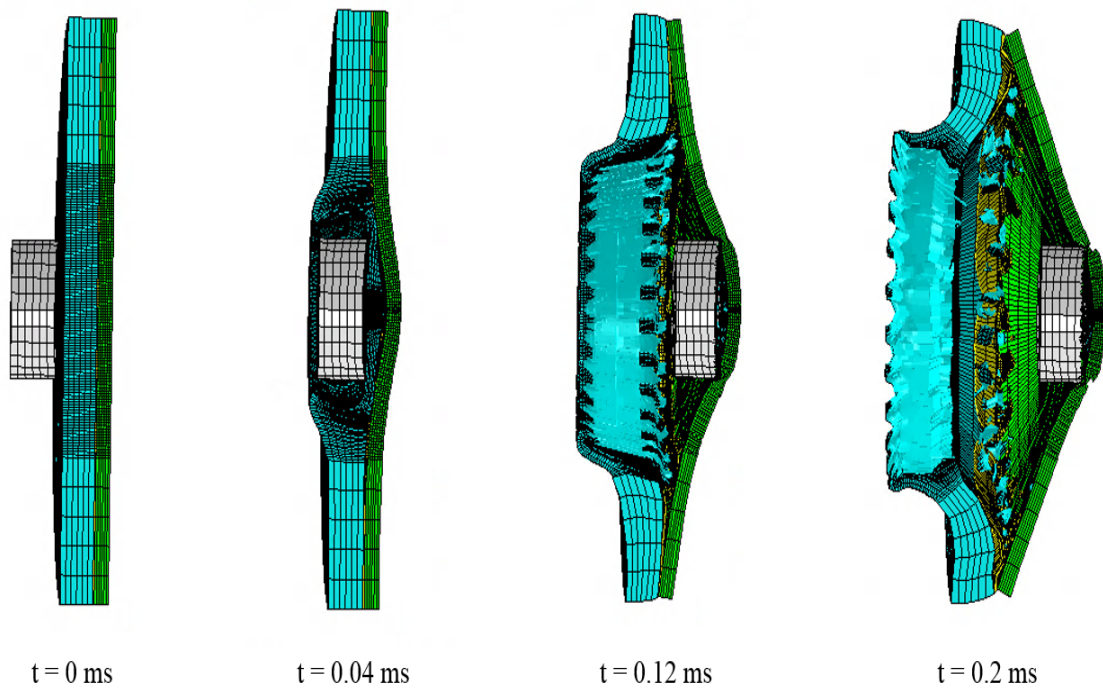


Figure 5.36: Damage progression for polyurea backed 4340 steel plate impacted by flat nose projectile at a velocity of 390 m/s.

5.7 Angle of impact

The study on the effect of the angle of impact is carried out in this work. Two scenarios - normal impact and an inclined impact with an inclination of 30° with the blank 4340 steel plate are simulated. The plots for the residual velocities and energy absorption are shown in figure 5.37 and figure 5.38 respectively. The behavior of the normal impact is as mentioned in section 5.3.1 but the inclined behavior is smooth with out any flattening in its energy absorption because the failure of the material involves both petalling and shear plugging right from the beginning and there is no transition in the failure modes. Figure 5.39 shows the damage progression of the blank plate in which it can be observed that the plate has a crack opening after initial contact with the tip of the projectile at $t=0.08$ ms where as at time step $t=0.16$ ms it starts to shear off resulting in its failure.

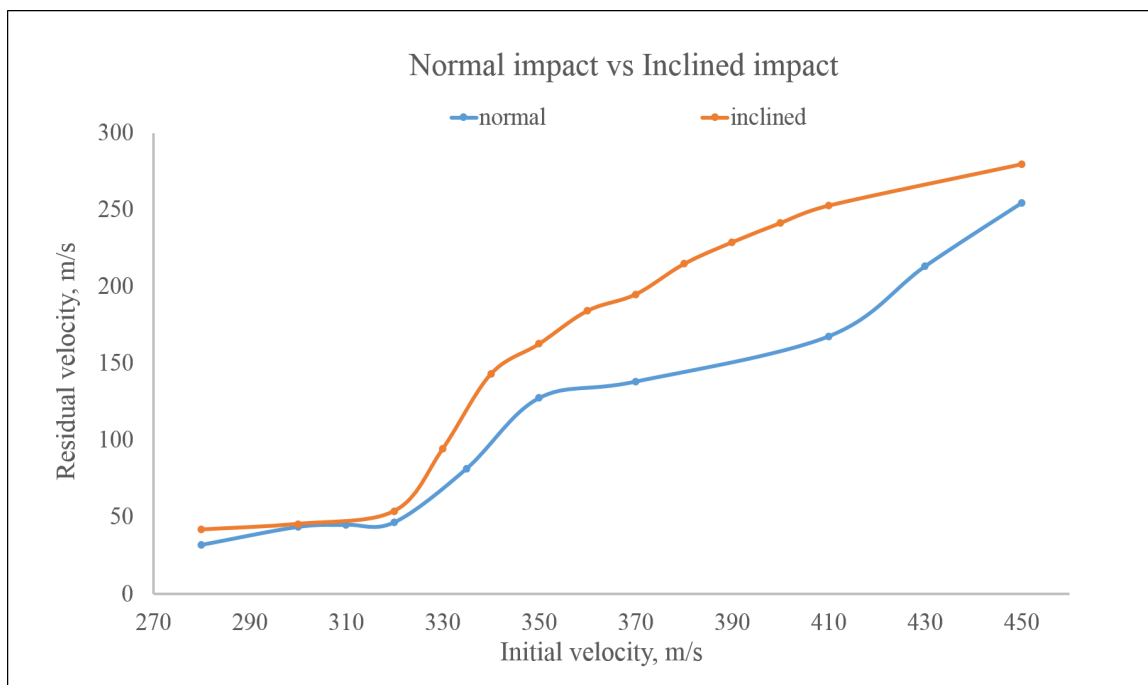


Figure 5.37: Residual velocities of the normal impact and inclined impacts of a pointed nose projectile on a blank steel plate

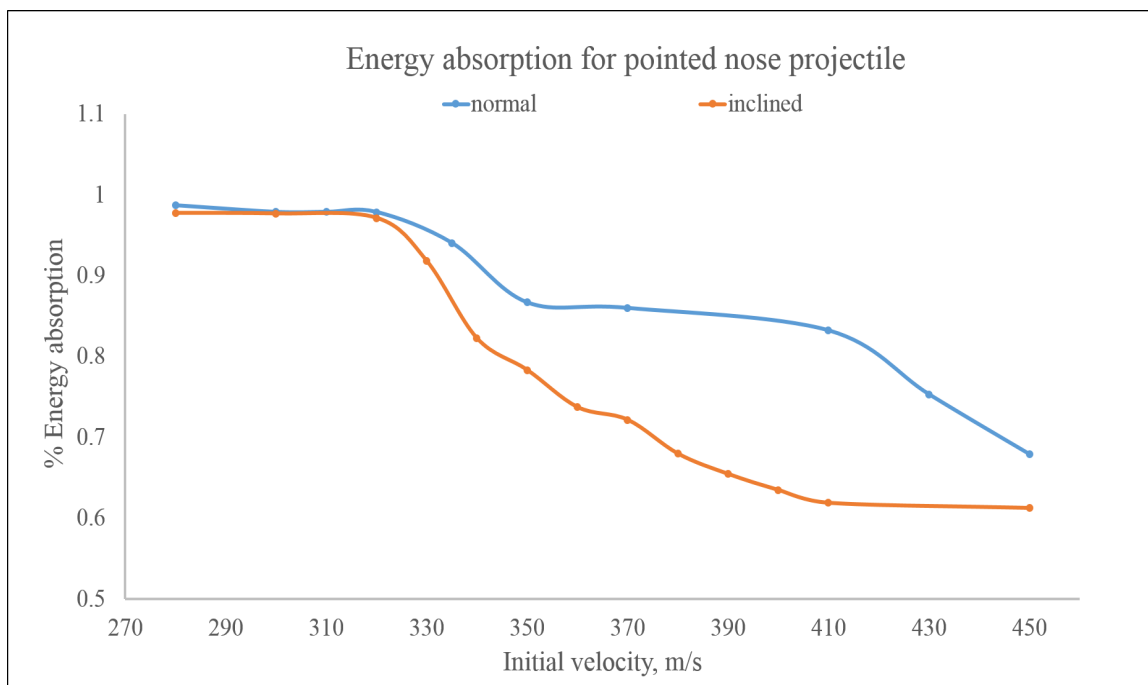


Figure 5.38: Energy absorption of the normal impact and inclined impacts of a blank steel plate impacted by pointed nose projectile.

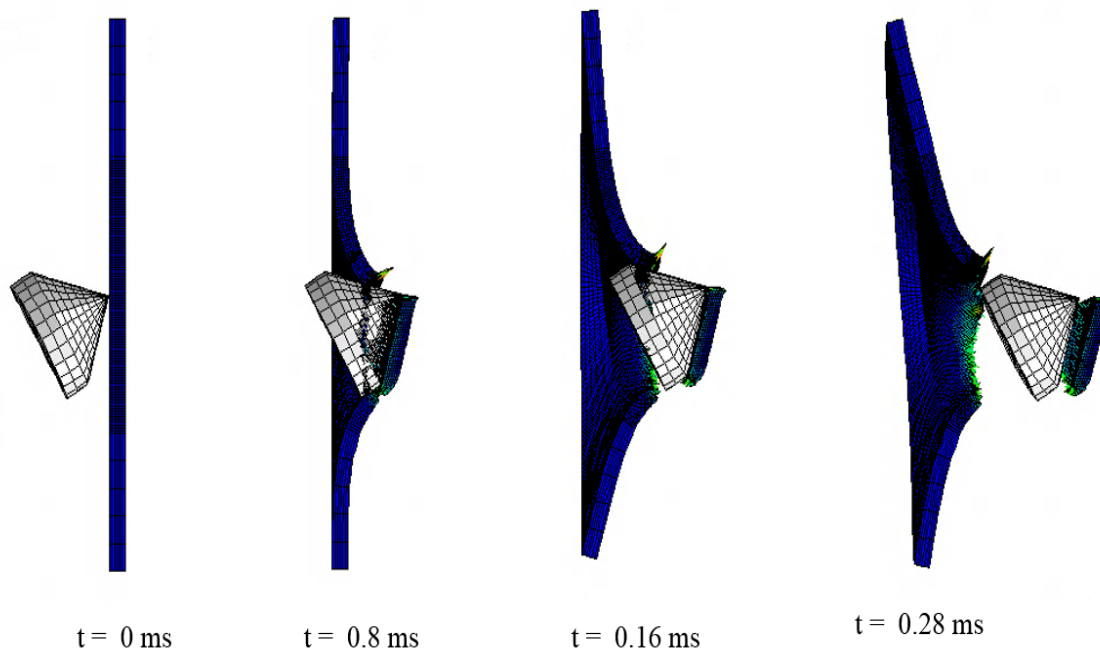


Figure 5.39: Section view of the damage progression of inclined pointed nose projectile impacting a blank 4340 steel plate at 360 m/s. Fringe plot is equivalent plastic strain, PEEQ

5.8 Sensitivity analysis

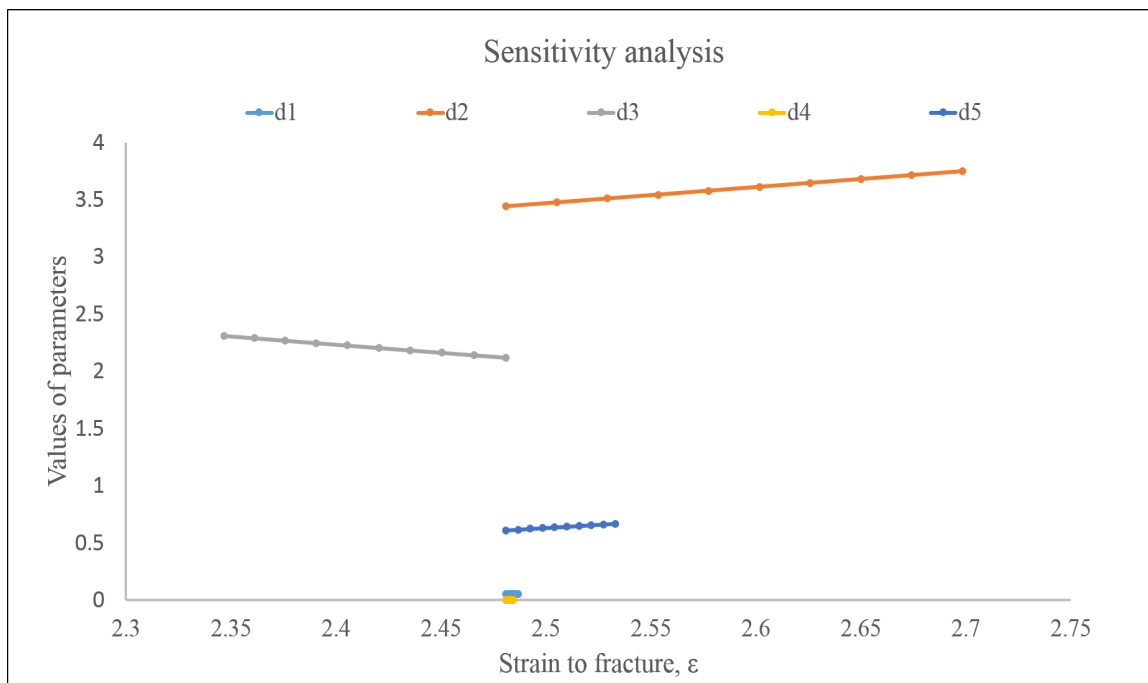


Figure 5.40: Change in strain to fracture with errors in the parameters

Sensitivity analysis was carried out to check the sensitivity of the fracture strain to the parameters $d_1 - d_5$ involved in its calculation. In this sensitivity analysis the fracture strain was directly linked with the ballistic limit of the material. The sensitivity is first estimated analytically in matlab by calculating the strain to fracture and how the parameters involved effect it. From the figure 5.40 it can be seen that parameter d_2 followed by parameter d_3 show a significant change in the fracture strain, while a small percentage change in the other parameters does not yield much of a difference to the fracture strain. This sensitivity was then checked through simulations and figure 5.41 shows how the fracture strains change with the change in the value of parameters d_2 and d_3 which in turn effects the ballistic limits, while parameter d_5 doesn't show much of an effect. This sensitivity may be due to the fact that magnitudes of parameters d_3 and d_4 are larger compared to that of others which in turn is effecting the fracture strain.

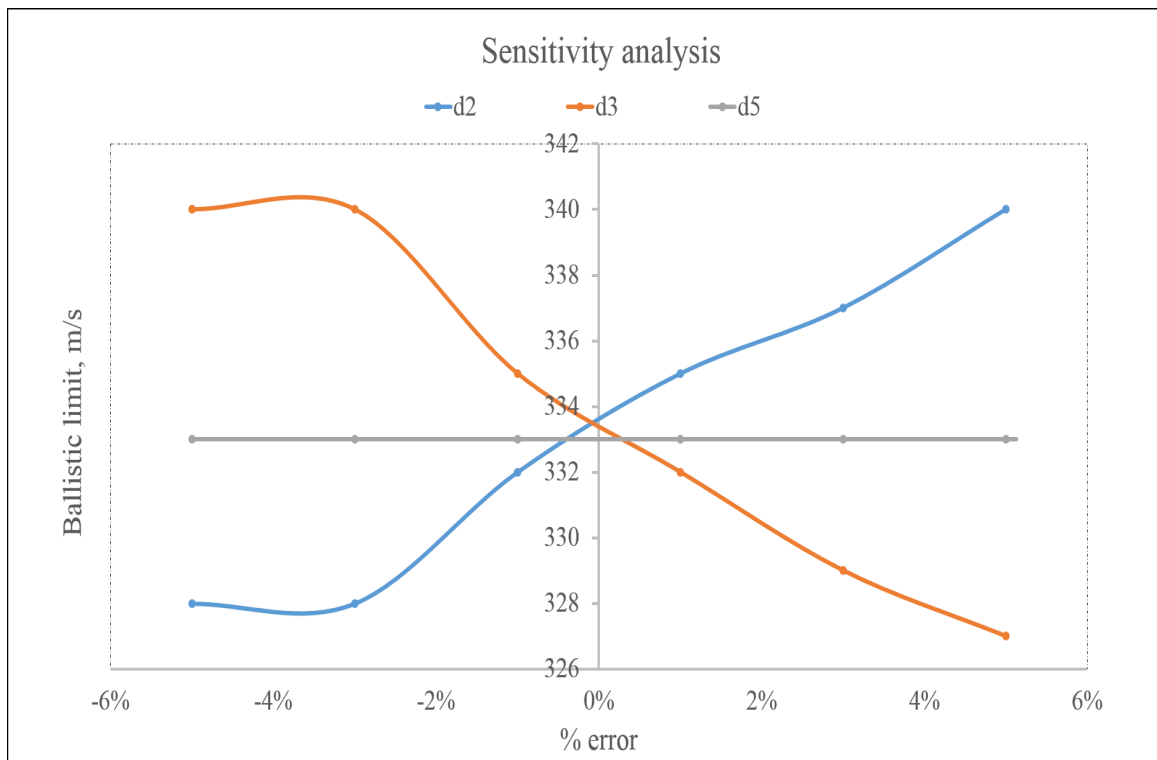


Figure 5.41: Change in the ballistic limits of the blank 4340 steel plate impacted by pointed nose projectile as a function of percentage error of the parameters.

CHAPTER 6: Summary and Conclusion

The effect of polyurea on the penetration resistance of 4340 steel plate impacted by different types of projectiles is studied. The effect of the orientation of the polyurea at the front, back and in between the plates is studied. The effect of the shape of the projectile on the overall energy absorption is studied.

The first scenario considered was of a pointed nose projectile, which was impacted on blank steel plate, polyurea backed plate, polyurea sandwiched plate and polyurea front plate. The ballistic limit of the blank plate was 335 m/s, which was increased by 10% to 370 m/s after adding the polyurea coating onto the back of the plate. Flattening in the energy absorption was observed in the middle which was accounted to the mode transition of the fracture [21].

The second scenario was jacket nose projectile which was impacted again on all the four scenarios. Of all the scenarios, the polyurea front showed to have the better energy absorption by increasing the ballistic limit by 11% from 370 m/s to 410 m/s. Both polyurea backed and polyurea sandwich did not show any effect, instead worsened the situation. A hint of petalling was seen in the fracture but a large shear plug was ejected during penetration.

The third scenario was with round nose projectile impacted on all four different plates. The ballistic limit of the blank plate is found to be 340 m/s which was increased by 2% to 350 m/s by adding polyurea on the back of the plate and by 9% to 370 m/s by adding the polyurea on to the front of the plate. There was no hint of petalling with round nose except for polyurea sandwich plate where the shear plug from the first steel plate might have caused the petalling in the second plate.

And in the final scenario, the flat nose projectile when impacted on blank steel

plate gave a ballistic limit of 330 m/s, which increased by 3% to 340 m/s from the polyurea coated on back, by 12% to 370 when polyurea was sandwiched between the plates and by 18% to 390 m/s when the polyurea was on the front, the highest of all. The polyurea was found to detach from the plate after the impact in polyurea sandwich and polyurea front which might have added for the penetration resistance.

The case of polyurea on the back side of the plate is seen to be effective only in the case of pointed nose projectile because of the petalling of the material during initial damage while in all the other cases where there is not much of petalling it is ineffective, the polyurea in the front is easily teared off by the pointed nose projectile thus showing no effect [22].

In the case of blunt projectiles like jacket nose, round nose and flat nose, the polyurea coating at the front alters the nose shape of the projectile impacting the plate and delays the failure of the material by damping down the kinetic energy of the projectile. The more blunt the projectile is, the more effect polyurea on the front side has on it [22].

REFERENCES

- [1] W. M. J. Liang Xue and T. Belytschko, "Penetration of dh-36 steel plates with and without polyurea coating,"
- [2] G. Johnson and W. Cook, "A constitutive model and data for metals subjected to large strains, high strain rates and high temperatures,"
- [3] E. Q. Sun, "Shear locking and hourglassing in msc nastran, abaqus and ansys,"
- [4] *Abaqus Analysis User's Guide.*
- [5] T. H. B. C. C. Y. C. R. M. Grujicic, B. Pandurangan, "Computational investigation of impact energy absorption capability of polyurea coatings via deformation-induced glass transition,"
- [6] R. B. Bogoslovov and R. G. C.M. Roland, "Impact-induced glass transition in elastomeric coatings,"
- [7] "Aisi 4340 alloy steel."
- [8] S. DJ, *Equations of states.*
- [9] G. Johnson and W. Cook, "Fracture characteristics of three metals subjected to various strains, strain rates, temperatures and pressures,"
- [10] S. N.-N. M.R. Amini, J.B. Isaacs, "Experimental investigation of response of monolithic and bilayer plates to impulsive loads,"
- [11] J. R.-M. R. P. A. J.R. Klepaczko, A. Rusinek, "Modelling of thermo-viscoplastic behavior of dh-36 and weldox 460-e structural steels at wide range of strain rates and temperatures, comparison of constitutive relations for impact problems,"
- [12] A. R. A. Arias, J.A. Rodriguez-Martinez, "Numerical simulations of impact behavior of thin steel plates subjected to cylindrical, conical and hemispherical non-deformable projectiles,"
- [13] A. M. F. F. M. O. Tamer El sayed, Willis Mock Jr, "Computational assessment of ballistic impact on a high strength structural steel/polyurea composite plate,"
- [14] T. H. B. C. C. Y. C. M. Grujicic, B. Pandurangan, "Computational investigation of impact energy absorption capability of polyurea coatings via deformation-induced glass transition,"
- [15] S. Nemat-Nasser and W.-G. Guo, "Thermo mechanical response of dh-36 structural steel over a wide range of strain rates and temperatures,"
- [16] S. Yadav and G. Ravichandran, "Penetration resistance of laminated ceramic/polymer structures,"

- [17] Y. V. C.M. Roland, J.N. Twigg and P. Mott, “High strain rate mechanical behavior of polyurea,”
- [18] J. Zukas, *Introduction to hydrocodes*.
- [19] S. B. Segletes, “An analysis on the stability of the mie-grüneisen equation of state for describing the behavior of shock loaded materials.”
- [20] G. T. M. Ronald E. Smelser and G. E. Mase, *Continuum Mechanics for Engineers*.
- [21] J. F. Kalthoff, “Failure methodology of mode-ii loaded cracks,”
- [22] W. S. I. Mohagheghian, G.J. McShane, “Impact perforation of polymer-metal laminates: Projectile nose shape sensitivity,”